

Goddard

NONSCANNING CLIMATE SENSOR STUDY

Prepared by:
James W. Hoffman
Ronald C. Grush
Space Instruments, Inc.

July 1989
Final Report for Contract Period
May 1987 to May 1989

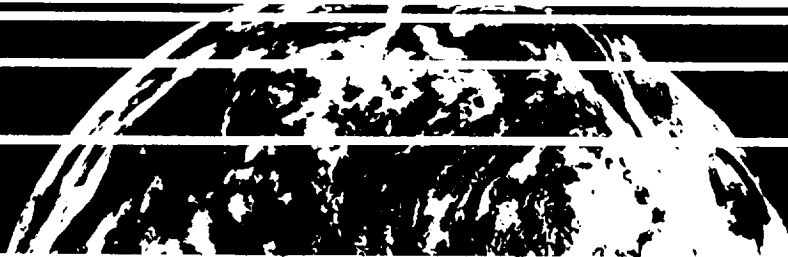
Prepared for:
Goddard Space Flight Center
Greenbelt, Maryland 20771

(NASA-CR-183506) NONSCANNING CLIMATE SENSOR
STUDY Final Report, May 1987 - May 1989
(Space Industries) 66 p CSCL 043

N92-11589

Unclass

83/47 0219528



**SPACE
INSTRUMENTS, INC.**

4403 Manchester Blvd.
Suite 203
Encinitas, CA 92024
(619) 944-7001



Report Documentation Page

1. Report No. 9	2. Government Accession No.	3. Recipient's Catalog No.	
4. Title and Subtitle NONSCANNING CLIMATE SENSOR STUDY		5. Report Date July 1989	
		6. Performing Organization Code	
7. Author(s) James W. Hoffman, Ronald C. Grush		8. Performing Organization Report No. SI89-R07JWH001	
9. Performing Organization Name and Address Space Instruments, Inc. 4403 Manchester Avenue, Suite 203 Encinitas, CA 92024		10. Work Unit No.	
		11. Contract or Grant No. NAS5-30090	
12. Sponsoring Agency Name and Address Dr. Albert Arking Goddard Space Flight Center Greenbelt, MD 20771		13. Type of Report and Period Covered Final Report May 1987-May 1989	
		14. Sponsoring Agency Code	
15. Supplementary Notes			
16. Abstract <p>The Nonscanning Climate Sensor represents a new instrument for climate research and global monitoring of the earth radiation budget.</p> <p>It contains a mosaic array of detectors which measures the outgoing radiation of the earth in all directions without the need for mechanical scanning. The goal is to eliminate all moving parts and obtain highly calibrated measurements for up to one solar cycle (11 years) without being susceptible to mechanical failure. Over set intervals of time, the angular measurements are integrated up to produce total reflected and emitted flux values from each target area on the earth. To achieve the required sensitivity while maintaining a flat spectral response, an improved dual cavity detector with digital control loop has been developed. The detector is self calibrating to maintain high precision over the life of the instrument.</p> <p>Prototype detectors and a complete set of electronics with a microprocessor controller have been fabricated and tested by Space Instruments, Inc. Measurements have demonstrated that the new detectors are more than an order of magnitude more sensitive than previous versions.</p>			
17. Key Words (Suggested by Author(s)) Climate, radiation budget, cavity detector, thermal detector		18. Distribution Statement	
19. Security Classif. (of this report) Unclassified	20. Security Classif. (of this page) Unclassified	21. No. of pages 64	22. Price

TABLE OF CONTENTS

	Page No.
1.0 Introduction	1
2.0 Performance Requirements	3
2.1 Top Level Requirements	3
2.2 Electronic Precision Analysis	4
2.3 Precision and Absolute Accuracy Error Budget	6
3.0 Instrument Design	10
3.1 Instrument Design Concept	10
3.2 Block Diagram	15
3.3 Concentric Versus Planar Configuration Tradeoff	15
3.4 Physical Parameter Estimates	17
4.0 Detector and Electronics Design	19
4.1 Detector Equation	19
4.2 Detector Module Design	22
4.3 Electronics Design	24
4.4 Control Loop Analysis	26
5.0 RADCON Computer Simulation	28
5.1 RADCON Program Description	28
5.2 RADCON Sample Run	30
6.0 Hardware Fabrication	34
7.0 S/W Development	36
7.1 Filter Program	36
7.2 CAPCOMM.ASM	37
7.3 TARGET.ASM Program	37
8.0 System Testing and Characterization	38
8.1 Test Configuration	38
8.2 Detector Characterization	39
8.2.1 Open Loop Detector Responsivity and Time Constant	39
8.2.2 Closed Loop Detector Responsivity and Time Constant	40
8.2.3 Detector Characterization Summary	40

8.3 Closed Loop dynamic Response	42
8.3.1 Detector Transfer Function	42
8.3.2 Step Input Response	44
8.4 Electronic Noise Measurements	47
8.4.1 Noise Measurements	47
8.4.2 Noise PD	49
8.4.3 Noise Versus Temperature	49
8.4.4 Summary	50
8.5 Detector to Detector Pattern Noise	51
8.6 Long Term Stability	52
8.7 Crosstalk	54
8.8 ROM Absolute Calibration	56
8.9 Performance Summary	57
9.0 Conclusions and Recommendation	58
10.0 Recommendations	58

LIST OF ILLUSTRATIONS

Figure		Page No.
2.1	Detector Precision Model	15
2.2	Sensor Precision VRS $A_c \cdot \text{IFOV}$	5
2.3	Sensor Precision Vrs Temperature Control	5
2.4	Instrument Precision and Absolute Accuracy	6
3.1	Earth Radiation Array Instrument	12
3.2	Earth Radiation Array Cross Section	13
3.3	Top View of Detector Array	13
3.4	Integral Baffle/Heatsink Structure	13
3.5	Shutter and Filter Mechanisms	14
3.6	Plan View of Dual Array	14
3.7	System Blocking Diagram	15
3.8	Planar Instrument Configuration	16
3.9	Concentric Vrs. Planar Size Comparison	16
4.1	Basic Operation of ACR Detector	19
4.2	ACR Detector	22
4.3	Detector Module - Exploded View	23
4.4	Electronics and Development System Block Diagram	25
4.5	Theoretical Step Response Output with IIR Filter, $A=23.344$	26
4.6	Theoretical Step Response Error with IIR Filter, $A=23.344$	27
4.7	Theoretical Output with IIR Filter, $A=23.531$	27
4.8	Theoretical Error with IIR Filter, $A=23.531$	27
5.1	Earth-Spacecraft Geometry	29
5.2	Field Aperture Geometry	29
5.3	RADCON Earth Pattern Outputs	29
5.4	Field Aperture Shapes	29
5.5	Common Aperture Size Vrs. Baffle Length	29
5.6	Wing Energy Vrs. Baffle Length	30
6.1	Dual Cavity Detector Fabrication	34
6.2	Detector Module	35
6.3	Electronics Unit	35
7.1	Real Time Display of Step Input Response with IIR Filter	37
8.1	Test Configuration	39
8.2	Responsivity and Time Constant Measurement - Det. 1	39
8.3	Closed Loop Responsivity - Det. 1	40
8.4	Temperature Coefficient Measurement	41
8.5	Detector Transfer Function	43
8.6	Detector Gain Vrs. Operating Point	44

8.7	Closed Loop Response to Step Input of Radiance - Det. 1	45
	Real Time Monitor Output	
8.8	Step Input Response - Det. 1	46
8.9	Step Input Response Vrs. Loop Gain	46
8.10	Step Input Response Vrs. Loop Integration	47
8.11	Time Outputs After Averaging	48
8.12	Noise Reduction by Sample Averaging	48
8.13	Noise PSD - Det. 1 Capped	49
8.14	Noise Vrs. Temperature	50
8.15	Detector to Detector Pattern Noise with Cold Plate	51
8.16a	10 Day Drift Test	53
8.16b	Minimum/Maximum Air Temperatures at San Diego Airport	53
8.17a	Electrical Crosstalk Test	54
8.17b	Detectors 2 and 3 Outputs During Crosstalk Test	54
8.18a	Crosstalk Test	55
8.18b	Crosstalk Detector Outputs	55
8.19	ROM Absolute Calibration	56

LIST OF TABLES

Table No.		Page No.
		4
		7
2.1	Top Level Instrument Requirements	8
2.2	Precision Error Budget	9
2.3	Absolute Accuracy Budget	17
2.4	Instrument Performance Requirements	17
3.1	Estimated Instrument Physical Parameters	18
3.2	Preliminary Weight Breakdown	28
3.3	Power Estimate	31
5.1	RADCOM Computer Simulation	42
5.2	Sample Run	57
8.1	Detector Responsivity and Time Constant	
8.2	Instrument Performance Summary	

1.0 INTRODUCTION

One of the primary objectives of earth radiation measurement programs is to accurately monitor long term fluctuations in the total flux leaving the earth's atmosphere.

Because energy is emitted and reflected in all directions, it is necessary to either measure the radiance at all angles or to use angular distribution models (ADM) to fill in missing angular measurements. In previous programs, mechanical scanning sensors have been used to obtain angular measurements in the crosstrack direction only. All of the other angular components have been estimated by means of ADMs. For the relected energy, the angular distribution can vary significantly depending on what type of scene is being viewed. Scenes such as clouds, ocean, desert, etc. have greatly varying reflectances as a function of angle.

An earth radiation instrument that makes radiance measurements in all directions would allow the direct summing or integration of these measurements to produce total flux values without the use of the angular models. Because these measurements must be made over very long periods of time (up to one solar cycle or 11 years) it is desired to have an instrument that operates without mechanical scanning. The elimination of the scanning parts increases the reliability and expected lifetime of the instrument significantly. The design of such a mosaic array type instrument was one of the primary objectives of this research project.

To obtain accurate measurements of the emitted and reflected flux from the earth/atmosphere system, it is necessary to have detectors that cover wide spectral regions (0.2 to 50 μ). Dual cavity radiometers have flat responses over the spectral range of 0.2 to 100 μ and maintain excellent stability and absolute accuracy due to the energy balance mode in which they operate. The output signal is a direct power measurement so there is no photon conversion efficiency that must be considered. Because the detector bridge circuit always operates at a null value the detectors are perfectly linear over their entire dynamic range. The detectors can be self calibrated by means of a reflective shutter. This eliminates the requirement for the instrument to view space, the sun, or blackbody sources for calibration. This allows frequent calibrations and greatly improves the final precision of the instrument on orbit.

Active cavity detectors were used in the wide field of view detectors on the ERBE nonscanning instrument which viewed the entire earth. Similar detectors have been used for many years for solar monitoring and are part of the World Radiometric Reference (WRR). None of these cavity detectors have the required sensitivity to accurately monitor small areas of the earth. To obtain 1% radiometric precision with 250 Km resolution requires an improved detector with a sensitivity at least 5 to 10 times better than that of previous cavity detectors. The second objective of this project, therefore, was to design an improved version of this detector with a sensitivity 10 times that of previous versions.

Previous dual cavity detectors have been built as single units with analog feedback control loops. For an instrument containing a large array of detectors this would be

impractical. A new electronics design employing an integral preamplifier located within each detector module and a digital control loop was designed. The digital control loop allows a single microprocessor to control and optimize the response for all of the detectors in the array. Implementing the compensation filter in software also allows different loop responses to be used for different modes of operation such as earth viewing and calibration.

During the Phase I feasibility study performed in 1986, a design concept was generated for the new detector and digital controller. Phase II of the SBIR project began in May 1987.

The objectives of the Phase II Nonscanning Climate Sensing project were:

1. To design, fabricate, and bench test an improved detector with new digital electronics and digital controller.
2. To complete a conceptual design of an entire nonscanning climate sensor.
3. To design a commercial version of the detector.

Phase II of the research project was completed in May 1989. All of the objectives of the project were successfully fulfilled. The detectors achieved more than 10 times improvement in responsivity and the digital control loop performed without flaw. Test measurements indicate that the overall stability of the new detector is on the order of 100 times better than the required value.

The system test results indicate that the long term precision and absolute accuracy of the final instrument should exceed the original performance objectives. The extreme accuracy and stability of the detectors shows that they also have commercial application as absolute radiometric references for laboratories, test chambers, and other flight instruments requiring accurate calibration. The overall instrument concept has been demonstrated to be feasible. The instrument has been named the Earth Radiation Array (ERA).*

* A patent application has been filed on the ERA.

2.0 PERFORMANCE REQUIREMENTS

2.1 TOP LEVEL PERFORMANCE REQUIREMENTS

Table 2.1 gives a list of top level requirements for the instrument. The instrument is designed in a modular fashion and can be optimized for any desired orbit. The nominal spatial resolution used for the baseline polar orbit Earth Radiation Array (ERA) was 250 Km by 250 Km. Higher resolution versions are possible which contain a larger number of detectors. Using the baseline ERA in a low earth equatorial orbit on the shuttle or space station would produce approximately 125 Km x 125 Km resolution. This would be beneficial for monitoring important energy transport mechanisms in the equatorial regions. In order to resample the data to coincide with standard earth reference grid patterns, approximately three samples per pixel are desired.

Because angular data from different orbits will be integrated to obtain outgoing flux measurements, individual footprints will not be spatially aligned. One objective is thus to have footprint patterns with aspect ratios as close to 1.0 as possible. The ability to shape each field of view for all pixels is one of the advantages of the ERA instrument. With mechanical scanners the earth curvature results in a greatly elongated footprint towards the edge of the earth.

To obtain a true measurement of total flux the spectral response of the instrument should be essentially flat from 0.2 to 50 μ and polarization should be minimized. The optimum way to obtain this is to use cavity detectors with emissivity greater than 0.999 at all wavelengths and no intervening optics. The baseline detector has an emissivity greater than 0.9999 from 0.2 to 100 μ .

The most important performance parameters for the instrument are the long term precision over a one month period and the absolute accuracy. The precision goal is 1% of the average earth radiance or approximately 1.4 W/M²*SR. The goal for the absolute accuracy, after integrating up the radiance values at all angles, is 1% of the average total flux or approximately 4 W/M². In the following sections, all of the noise and drift sources within the detector and electronics are analyzed and error budgeted to meet these design goals. System tests on the breadboard model are then used to verify that each of the error allocations can be met.

TABLE 2.1

TOP LEVEL INSTRUMENT REQUIREMENTS

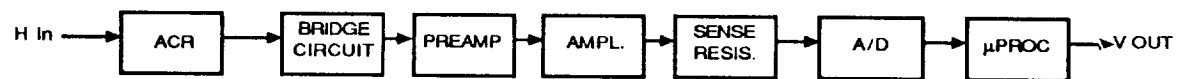
PERFORMANCE	SELECTABLE
ORBIT	250 KM x 250 KM
SPATIAL RESOLUTION	3 SAMPLES/PIXEL
SAMPLE RATE	0.8 TO 1.2
FOOTPRINT ASPECT RATIO	TOTAL - 02 TO 50 μ
SPECTRAL BANDPASS	SW - 0.2 TO 3.5 μ
POLARIZATION	NEGLECTIBLE
LINEARITY	1%
PRECISION (OVER 1 MONTH)	1.4 W/M ² *SR (1% EARTH RADIANCE)
ABSOLUTE ACCURACY	4 W/M ² (1% TOTAL FLUX)
CALIBRATION METHOD	REFLECTIVE SHUTTER
WFOV CHANNELS	TOTAL, SW, CONTAMINATION
LIFETIME	11 YRS (1 SOLAR CYCLE)

2.2 ELECTRONIC PRECISION ANALYSIS

In order to determine the required sensitivity for the new detector, an electronic precision model was constructed by SI which contains all of the electronic noise and drift terms. It was assumed at this point that the instrument thermal control system and the integral baffle/heatsink design will maintain the thermal fluctuations and drifts below these levels between shutter calibrations. Figure 2.1 shows the terms included in the electronic precision model.

A curve of electronic precision versus normalized input power is shown in Figure 2.2. The curve is plotted for the JPL/ACRIM detector used in solar monitoring along with the new Si detector with nominal and worse case noise and drift components. The normalized power inputs for the instrument range from $3.1 \text{ E-}7 \text{ (M}^2\text{*SR)}$ at the edge of the earth to $10.9 \text{ E-}7$ at nadir. If the 1% radiance requirement of $1.4 \text{ W/M}^2\text{*SR}$ is equally apportioned between electronics and thermal effects, the electronics requirement is $1.0 \text{ W/M}^2\text{*SR}$. It can be seen that this can be easily met with nominal performance.

Figure 2.3 shows the sensor precision as a function of electronics heatsink temperature control. Even using worse case errors, the precision requirements can still be met over the entire array if the electronics temperature is controlled to better than 0.6 degree. To provide a safety margin the temperature of the electronics will be controlled to better than 0.2 °C.



DRIFTS

- HEATSINK TEMP DRIFT BETWEEN SHUTTERING
- STRAY RADIATION
- RESISTOR TIME DRIFT
- V OFFSET TEMP DRIFT
- I OFFSET TEMP DRIFT
- V OFFSET TIME DRIFT
- R TIME DRIFT

RANDOM NOISES

- JOHNSON NOISE
- INPUT NOISE
- SHOT NOISE IN BIAS
- JOHNSON NOISE
- A/D QUANTIZ A/D NOISE
- μ P QUANTIZ

FIGURE 2.1. DETECTOR PRECISION MODEL

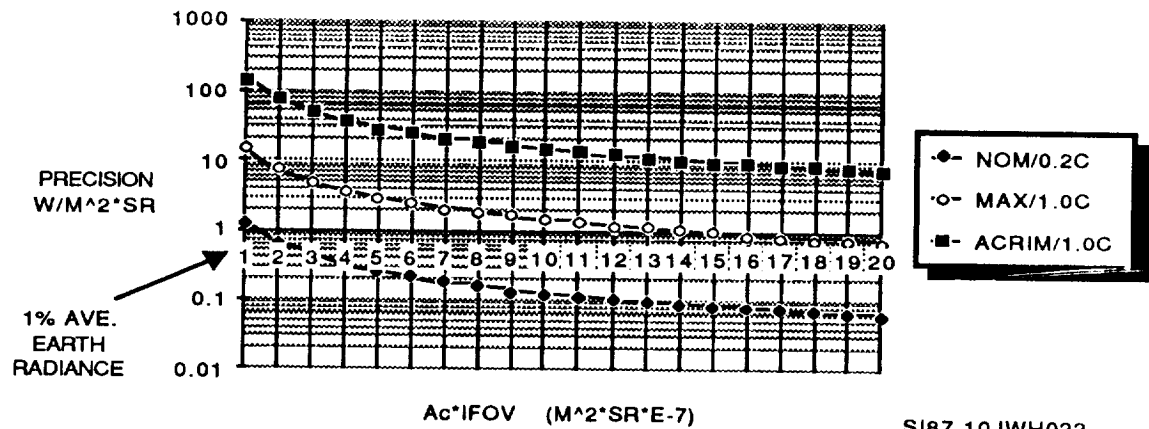


FIGURE 2.2. SENSOR PRECISION VRS. AcIFOV

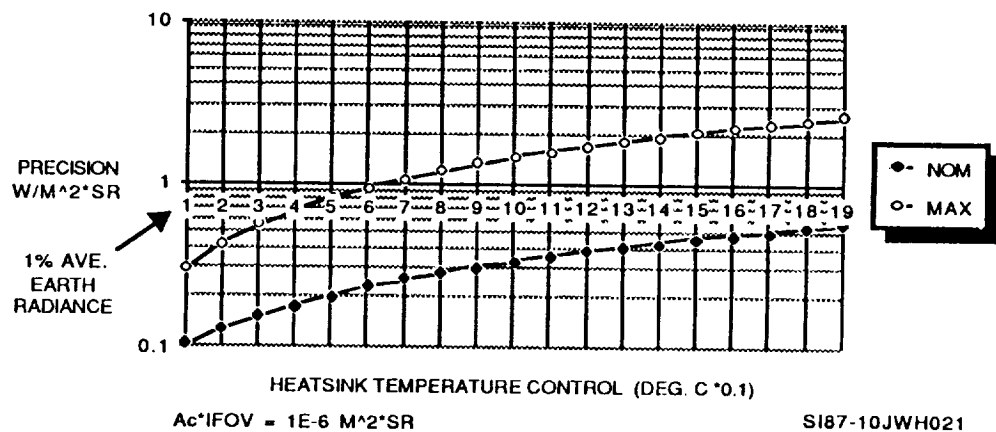
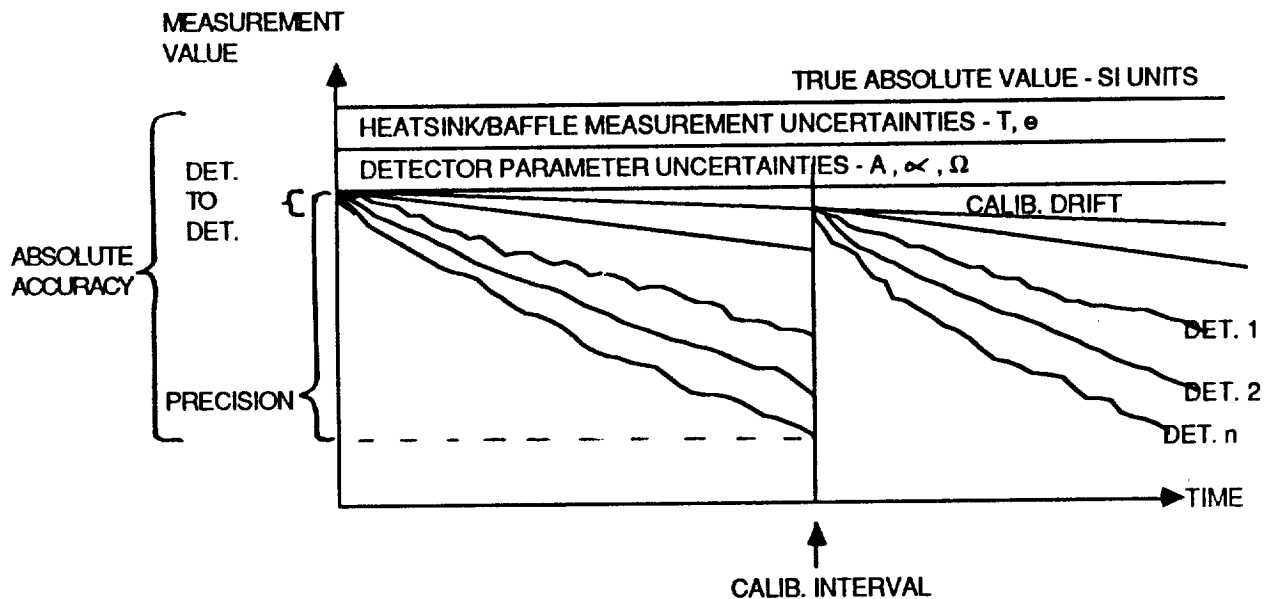


FIGURE 2.3. SENSOR PRECISION VRS. TEMPERATURE CONTROL

2.3 PRECISION AND ABSOLUTE ACCURACY ERROR BUDGET

Figure 2.4 shows a graphical explanation for the primary biases and drifts contained in the precision and absolute accuracy measurements. Everything is referenced to the true absolute value in SI units, which is constant over all time. The absolute accuracy obtainable is dependent on the uncertainty in measuring the collecting area and field of view of each detector and the temperature and emissivity of the heatsink. These represent offsets which are approximately constant with time. Electronic and thermal drift errors increase with time but are corrected for during shutter calibration. The precision of the instrument represents the RSS of all drift terms between calibrations plus the RSS of all noise terms. The averaging of samples and the summing of all of the detectors in the array to produce an integrated flux value reduce the random noise errors significantly. The drift terms thus represent the major components in the precision budget. At the bottom of Figure 2.4 is the equation for the measurement of scene radiance.

PRECISION GOAL = 1% OF NOMINAL EARTH RADIANCE OVER 1 MONTH (= 1.4 (W/M²,SR)
 ABSOLUTE ACCURACY GOAL = 1% OF NOMINAL EARTH FLUX = 4(W/M²)



$$N_{\text{SCENE}} = N_b \cdot \Delta P_h / a \cdot A \cdot \Omega + K \cdot \Delta N_b + \Delta \Sigma P_{lp} / a \cdot A \cdot \Omega$$

SI88-12JWH003

FIGURE 2.4

INSTRUMENT PRECISION AND ABSOLUTE ACCURACY

Table 2.2 shows the precision error budget for the ERA. The budget assumes that approximately 100 samples in times will be averaged to smooth out the electronic noise. Assuming Gaussian noise, this reduces the noise by a factory of approximately ten. The budget assumes that angular measurements from the 85 detectors will be summed together over a period of time to produce one flux measurement. The random detector to detector pattern noise will thus be reduced by the square root of 85. The drift values shown assume two calibrations per 100 minute orbit. The maximum drift period is thus on the order of 25 minutes. Allowing 0.3% for this long term detector drift translates into a drift requirement of 5.3 counts per minute. The conversion from radiance units to count levels out of the μ processor was done at the nominal earth level of 140 W/M²*SR or 22,000 counts. The error budget sums to 0.6% and thus provides considerable margin in meeting the overall precision goal of 1%.

TABLE 2.2
PRECISION ERROR BUDGET

GOAL = 1% OF NOMINAL EARTH RADIANCE OVER ONE MONTH = 1.4 (W/M²SR)

	BUDGET VALUE %	2 σ OUTPUT COUNTS		INDIVID. REQR. 1 σ OUTPUT CTS
		AFTER AVE.	BEFORE AVE.	BEFORE AVE.
(USE 2σ VALUE FOR 95%)				
•NOISE (DET. + PREAMP + SHOT + JOHNSON + QUANT. + DAC) (AVE. 100 TIME SAMPLES)	0.2	44	440	220
•DET. TO DET. RANDOM PATTERN NOISE (AVE. 85 DETECTORS)	0.2	44	400	200
RSS OF RANDOM COMPONENTS	0.28	62	600	300
			<u>DRIFTS CTS</u>	<u>DRIFT RATE</u>
•DET. DRIFT (OVER 1/2 CALIB INTERVAL OF 25 MIN)	0.3		66	5.3 CTS/MIN
•CALIB. DRIFT (DUE TO CONTAMIN. - OVER 1 MO.)	0.01		2	2 CTS/MO.
•CHANGE IN STRAY POWER LOSSES BETWEEN CALIB. & MEAS.	0.05		11	11 CTS/CALIB
•DRIFT IN BAFFLE/HEATSINK RADIANCE BETWEEN CALIB. & MEAS.	0.05		11	11 CTS/CALIB.
RSS OF DRIFTS	0.31			
SUM OF 2 σ NOISE + DRIFTS	0.59%			

*NOMINAL EARTH LEVEL = 22,000 COUNTS OUT OF μ P

SI89-01JWH018

The goal for the absolute accuracy of the instrument is 1% of the nominal earth flux or approximately 4 W/M^2 . The major sources of error are the baffle/heatsink emissivity and temperature and the detector collecting area and field of view. The values shown assume that the detector collecting area diameter can be measured to 0.2 mils under a microscope and the baffle length distances which determine the detector field of view can be measured to 2 mils. Summing the RSS of the random measurement errors with the total drifts from the precision budget gives an estimated absolute accuracy of 0.65% or 2.6 W/M^2 . This level of absolute accuracy has never been obtained with an earth radiation instrument to date. It will allow extremely accurate monitoring of the monthly fluctuations in the earth radiance measurements.

TABLE 2.3
ABSOLUTE ACCURACY BUDGET

GOAL = 1% OF NOMINAL EARTH FLUX = $4 \text{ (W/M}^2\text{)}$		
RANDOM ERRORS	BUDGET VALUE %	INDIV. REQD.
•BAFFLE TEMP. MEAS., T_B (OVER AREA VIEWED BY DET.)	0.05	0.04 °C
•BAFFLE EMISSIVITY KNOWLEDGE, ϵ_b (SPECTROMETER ACCUR.)	0.10	0.1%
•DETECTOR COLLECTING AREA, A_c (APERTURE DIMENS. MEAS. TO 0.2 MILS)	0.13	0.2 MILS
•DETECTOR FIELD OF VIEW, Ω (BAFFLE LENGTH MEAS. TO 2 MILS)	0.08	2 MILS
•DETECTOR CAVITY ABSORPTANCE, α (6 REFLECTIONS)	0.002	0.99988
•DETECTOR RANDOM ERRORS (FROM PRECISION BUDGET)	0.28	SEE PRECISION BUDGET
RSS	0.34	
<u>DRIFTS</u>		
•ALL DRIFTS (FROM PRECISION BUDGET)	0.31	SEE PRECISION BUDGET
SUM OF RANDOM ERRORS + DRIFT	0.65% 2.6 W/M^2	

S189-01JWH022

A summary of the performance requirements for the instrument is given in Table 2.4. This table takes the requirements from the previous two tables and translates them into quantities that can be directly measured with the breadboard hardware. The results from these tests will be compared with the requirements in section 8.0.

TABLE 2.4
INSTRUMENT PERFORMANCE REQUIREMENTS

NO.	PARAMETER	PERFORMANCE BUDGET	REQUIREMENT
1	RESPONSIVITY		1.5 V/W
2	NOISE -1 SIG.	0.1% NOM. (AFTER AVE. 100 SAMPLES)	220 CTS
3	DET. TO DET. VAR. -1 SIG.	0.1% NOM. (AFTER SUMMING 85 DETS)	200 CTS
4	DRIFT	0.3% NOM. OVER 1/2 CALIB. INTERVAL	5.3 CTS/MIN.
5	BAFFLE TEMP. DRIFT	0.05% NOM. (BETWEEN CALIB.)	0.05 °C/HR.
6	SETTLING TIME	28 SEC (TO 1%)	28 SEC.
7	DATA DUTY CYCLE		95%

NOTES: 1) NOISE AT INPUT TO μP IS ONLY $\approx \pm 1-3$ COUNTS

SI89-01JWH017

A comparison is often made between the accuracy of the dual cavity detectors when used for earth measurements versus when they are used for solar measurements. When the detectors are looking at the sun, the sun radiance is 5 orders of magnitude greater than the baffle radiance. This means that the baffle radiance terms can be ignored in the equation shown in Figure 2.4. Also, in solar measurements, the sun is stationary and a shutter calibration can be taken with every measurement. The detector is therefore operating in a chopped mode with calibrations approximately every 25 seconds versus every 25 minutes for a moving earth scene. All drift terms, which are the major error sources, are thus reduced by a factor of 60. Lastly, the solar energy is colimated and thus the field of view is known exactly by the sun/earth geometry. The error in computing the field of view is thus eliminated. When used in a solar monitoring mode, the ERA detector will thus achieve a precision and absolute accuracy significantly better than 1%.

3.0 INSTRUMENT DESIGN

3.1 INSTRUMENT DESIGN CONCEPT

Figure 3.1 shows an artist's concept of how the Earth Radiation Array would look on orbit. In this version of the instrument, 85 cavity detectors view their respective fields of view through a common aperture. This aperture, and a surrounding sunshade (not shown) eliminate direct solar loading at all but earth grazing angles. A CAD drawing of the instrument is shown in Figure 3.2. The ERA is approximately 32 inches on each side and 22 inches high without the sunshade. A plan view showing the arrangement of the 85 detectors is shown in Fig. 3.3.

Each detector module contains a field limiting aperture and a baffle that is an integral part of the common heatsink of the instrument. This common heatsink provides the temperature stability required to obtain the required long term precision. The proposed design features a CNC milled multilayer sandwich housing which is brazed into a monolithic mass prior to final machining. Each layer of the assembly contains a cavity for one half of the baffle structure configured for the detector field of view residing in that layer. The other half of the cavity resides in the bottom of the adjoining layer. The two cavities thus define the desired baffle system after brazing. There are seven such layers to be manufactured in the 85 detector design. Each layer will have lightening holes and milled out sections to reduce the overall mass of the housing. These lightening regions will be optimized with complex finite element thermal and structural modeling. A sketch of the integrated baffle design is shown in Figure 3.4.

A Suprasil dome filter is alternately placed in and out of the common aperture to obtain shortwave (0.2 to 3.5 μ) measurements along with the total measurements. This filter is cycled in and out three times per nadir pixel dwell time. Thus, the sample rate in both the total and short wave measurements is at least three times the Nyquist rate. This allows accurate resampling of the resultant data to any desired earth reference grid pattern. Both the filter and the calibration shutter will be activated by drive mechanisms such as the modified Geneva drives shown in Figure 3.5. The WFOV detectors will have their own calibration shutter mechanism.

Another proposed method of operation is to fly 2 identical ERAs on the same platform to eliminate moving the filter during normal operation. One would take SW measurements and the other total wavelength measurements. Each ERA could make either measurement and if one failed, the other could be used to make both measurements by cycling the filter. If the 2 ERAs were packaged as a single instrument to minimize volume, the overall detector arrangement would look as shown in Figure 3.6.

A highly reflective spherical shutter is inserted over the central aperture several times per orbit to calibrate the cavity detectors. This allows each detector to view heatsink temperature and null out any electronic drifts in the bridge amplifier circuit or thermal drifts in the heatsink. This provides the optimum calibration as both the primary and

reference cavities see the same temperature. if 2 ERAs are flown, one can occasionally be operated in a "chopped" mode by cycling the shutter in order to provide a check on the stability of the other.

Each detector module contains an integral preamplifier so that the signal going to the electronics unit has sufficient gain and is insensitive to stray capacitance and EMI. The electronic leads are routed through a central opening to the electronics boards at the top of the instrument. Heat from the electronics unit and heatsink is routed via conduction to the thermal louver on the space viewing side of the instrument. If no space view is available the heat is routed to the spacecraft thermal interface plate. The heatsink contains an active thermal control system and sufficient mass to maintain temperature fluctuations between calibrations to a level that is below the electronic drift during this same period.

In addition to the array detectors there are wide field of view (WFOV) detectors that view the entire earth. These detectors measure whole earth radiation in the total and short wavelength bands. There is also a contamination check detector which remains sealed and is only opened periodically to check for change in transmittance due to contamination. A contamination cover is designed to seal the unit during launch and during on orbit refurbishing of the satellite. This cover is integral with the sunshade that rejects the sun during terminator crossings at sunrise and sunset.

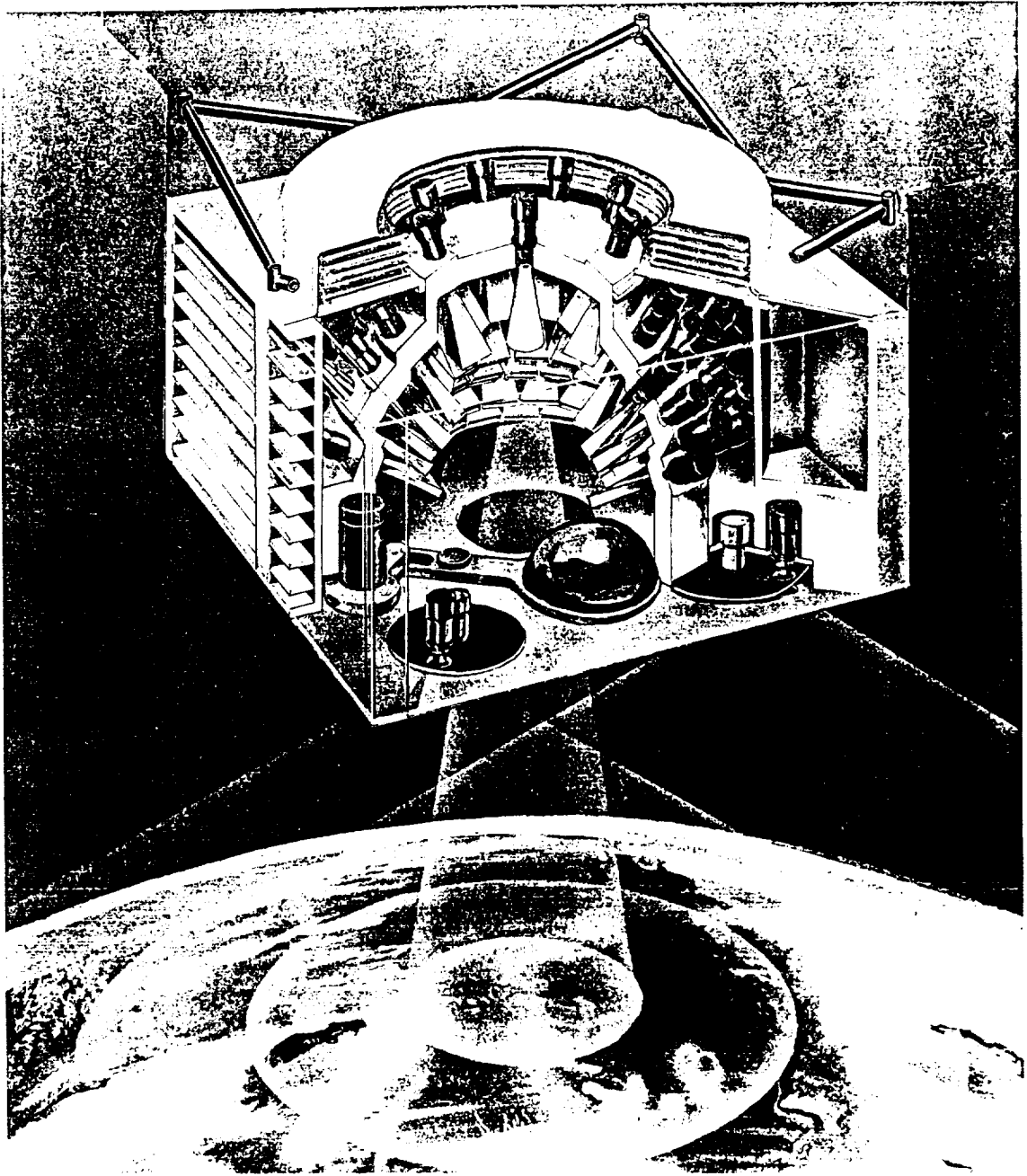


FIGURE 3.1. EARTH RADIATION ARRAY INSTRUMENT

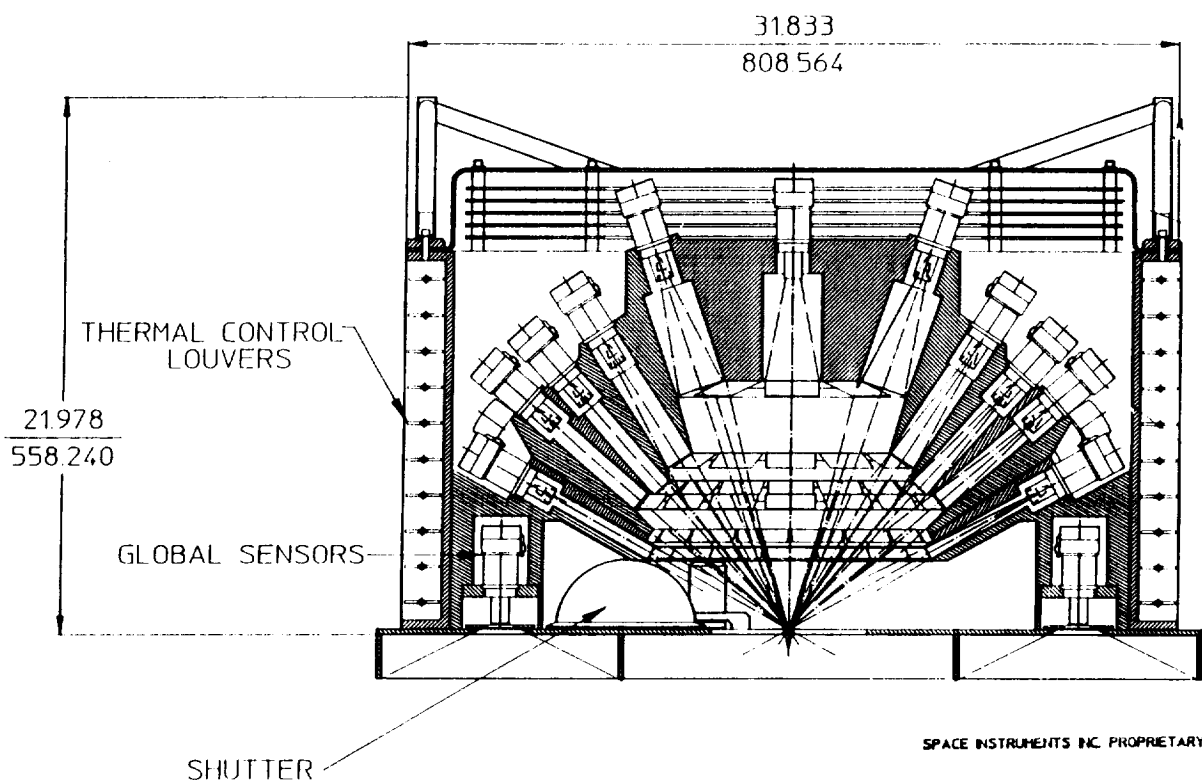


FIGURE 3.2. EARTH RADIATION ARRAY CROSS SECTION

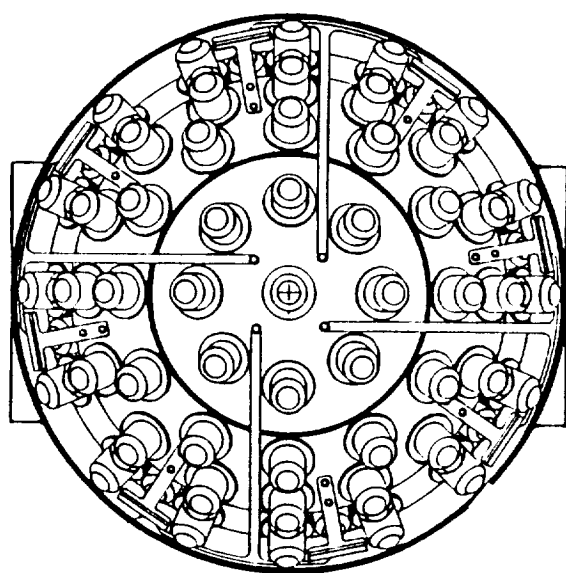


FIGURE 3.3
TOP VIEW OF DETECTOR ARRAY

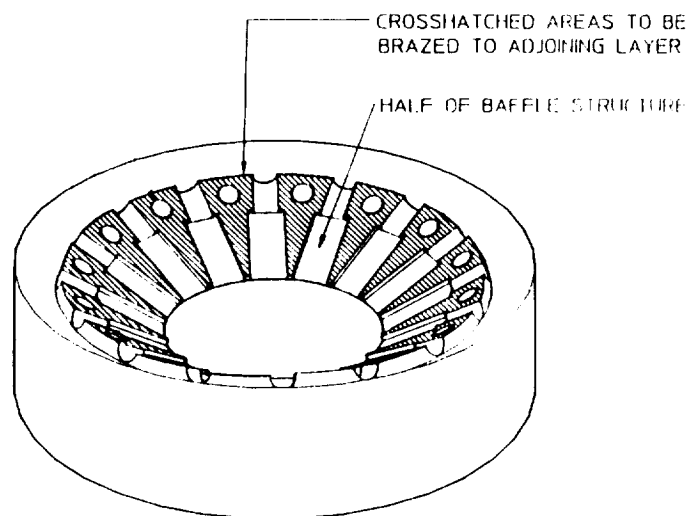
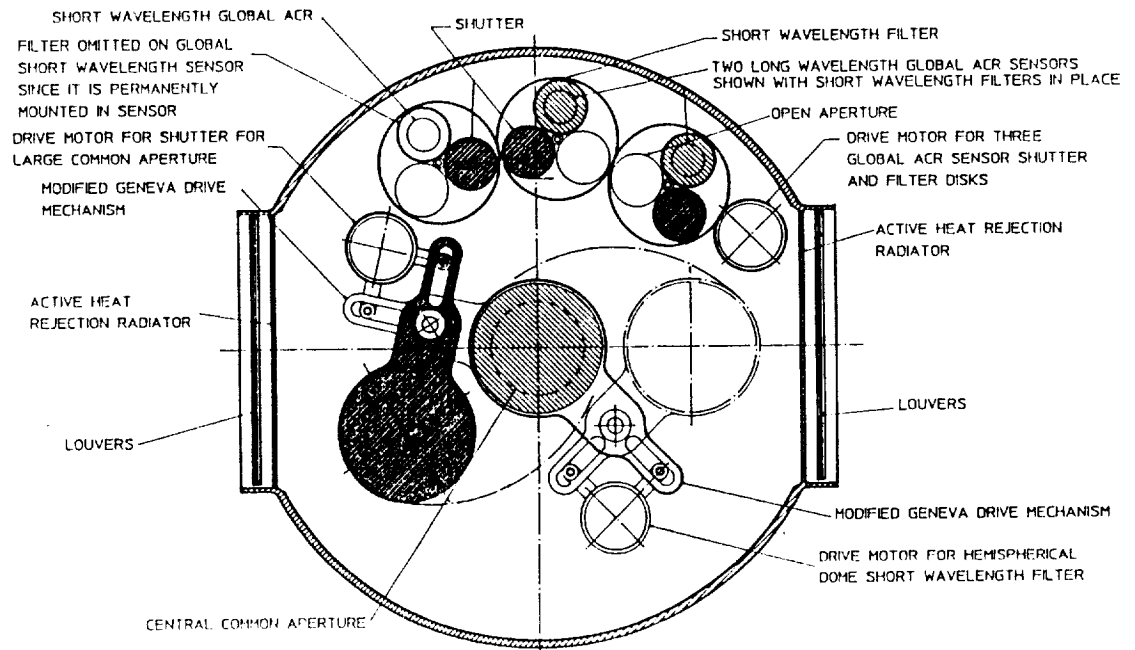


FIGURE 3.4
INTEGRAL BAFFLE/HEATSINK
STRUCTURE

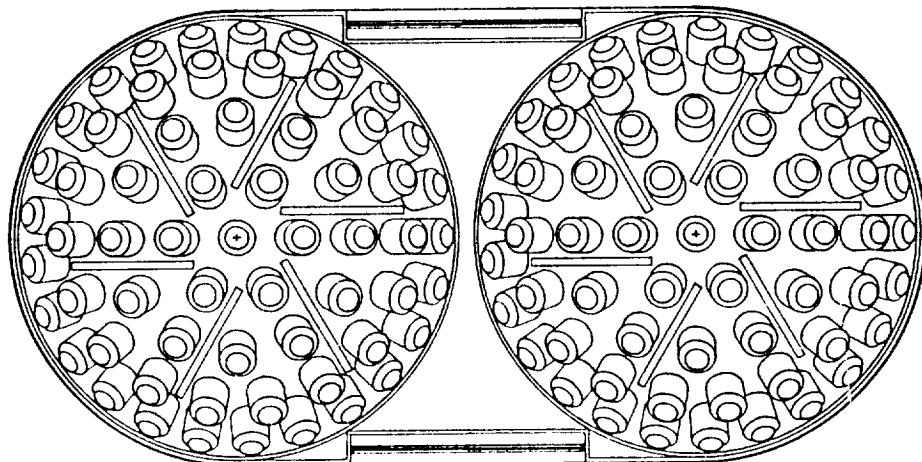


SPACE INSTRUMENTS INC. PROPRIETARY

SI87-12JWH010

FIGURE 3.5

SHUTTER AND FILTER MECHANISM



SPACE INSTRUMENTS INC. PROPRIETARY

FIGURE 3.6

PLAN VIEW OF DUAL ARRAY

3.2 BLOCK DIAGRAM

An overall system block diagram of the ERCA is shown in Figure 3.7. The dashed line represents scene energy from the Earth/atmosphere coming into the detectors. The energy is converted in the detector to a temperature change which is measured differentially with respect to the temperature of the heatsink as seen by the reference detector. A digital control loop is implemented in software by a microprocessor to close the loop via a heater located in the detector. All of the software required for the control loop and the data processing and formatting is stored permanently in PROM memory and is downloaded into working RAM memory upon startup. The electronics also generates correct voltages and timing signals for the drive mechanisms which control the contamination cover, the main shutter, the WFOV shutters and the spectral filter drive for the main array.

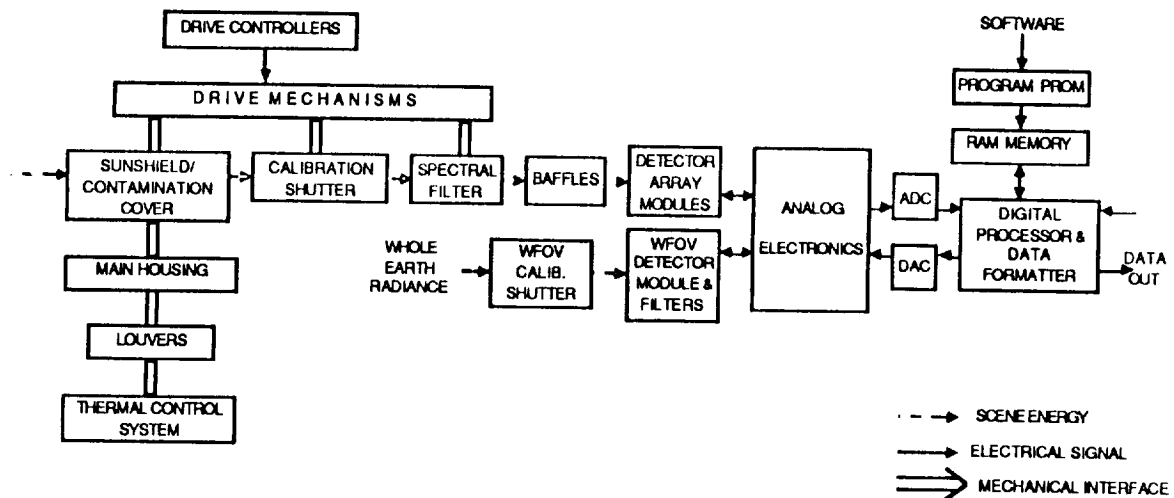
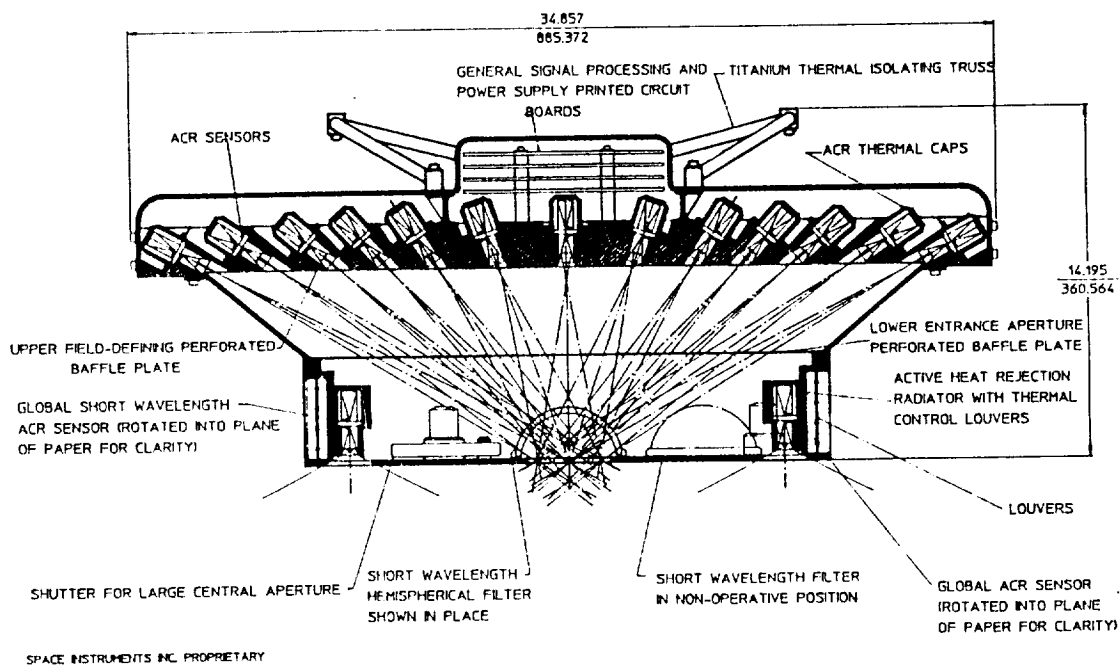


FIGURE 3.7. SYSTEM BLOCK DIAGRAM

3.3 CONCENTRIC VERSUS PLANAR CONFIGURATION TRADEOFF

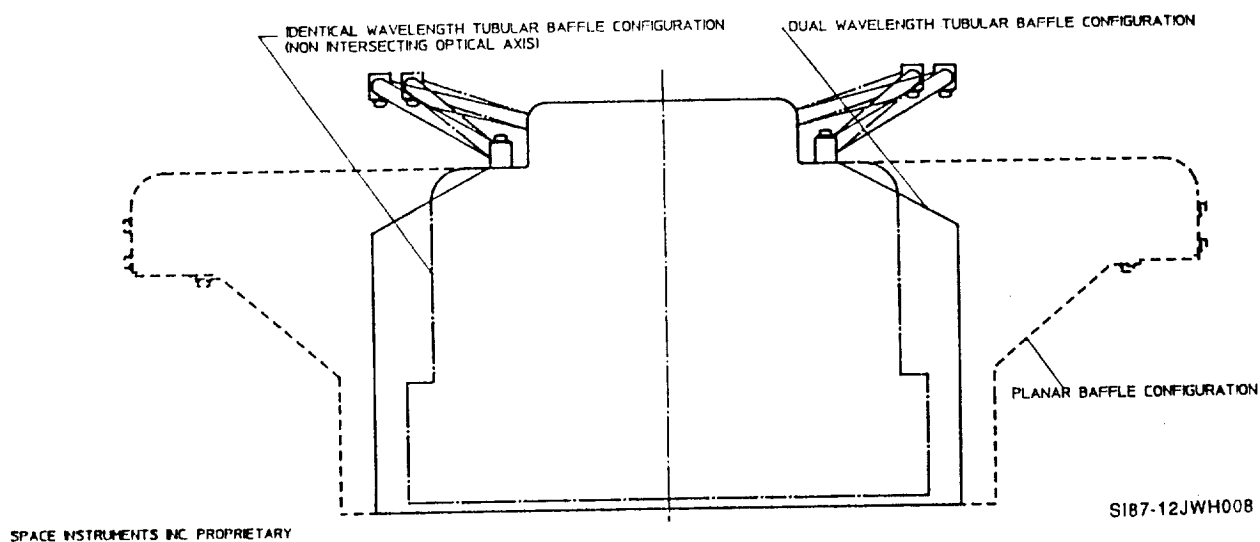
Early in the research project two different instrument configurations were considered. The first was a planar configuration in which all detectors were mounted on a flatplate. This configuration has the advantage of being simpler to manufacture. All of the field apertures can be machined into a single aperture plate. The fabrication of the thermal heatsink becomes a straight forward task. The size and shape of all of the field apertures can be derived via computer simulation and input to a numerically controlled milling machine. The RADCON computer simulation which will be described in section 5.0 contains the capability to generate the size and shapes of these field apertures automatically. A preliminary CAD layout of such a Planar configuration is shown in Figure 3.8.

The disadvantage of the Planar instrument approach is the large size of the instrument it produces. A comparison of the size of the Planar configuration with the baseline concentric configuration was performed. The Planar configuration produced a significantly larger diameter instrument. A comparison of the two outlines is shown in Figure 3.9. The outline for a third configuration with minimum volume but non-intersecting detector optical axes is also shown. A secondary problem with the Planar configuration is that for the same heatsink thermal mass the headsink is much larger and thinner and would therefore have larger thermal gradients. For these reasons, the concentric design approach was adopted for the baseline ERA design.



SI87-12JWH005

FIGURE 3.8. PLANAR INSTRUMENT CONFIGURATION



SI87-12JWH008

FIGURE 3.9. CONCENTRIC VRS. PLANAR SIZE COMPARISON

3.4 PHYSICAL PARAMETER ESTIMATES

An estimate of the physical parameters and output data rate for the ERA is given in Table 3.1. The output data rate is after smoothing the high μ processor sample rate to 4 samples/pixel for transmission to ground.

TABLE 3.1

ESTIMATED INSTRUMENT PHYSICAL PARAMETERS

NUMBER OF DETECTORS (IN MAIN ARRAY)	85
WEIGHT (Kg)	100
VOLUME (M ³)	0.6
POWER (W)	130
COOLING METHOD	LOUVERS OR CONDUCTION
CLEAR FOV REQUIRED	FULL EARTH (± 62 DEG)
PLATFORM FOOTPRINT AREA (M)	0.9 X 0.9
OUTPUT DATA RATE (Kbps)	0.36

A preliminary weight breakdown for the polar orbit instrument with 85 detectors is given in Table 3.2. Most of the weight resides in the main thermal housing and baffle assembly. The design of this assembly will be completed after a complete thermal analysis has been performed.

TABLE 3.2

PRELIMINARY WEIGHT BREAKDOWN

ITEM	UNIT WEIGHT	NO.	WEIGHT
DETECTOR MODULE	.459	88	40.37
MAIN THERMAL HOUSING (1.)	67.15	1	67.15
SHUTTER ASSEMBLY	2.88	2	5.6
LOWER PLATE OF MAIN HOUSING	28.9	1	28.9
RADIATION PANELS BEHIND LOUVERS	6.0	2	12.1
LOUVER CONTROL MECHANISMS	3.0	2	6.0
ELECTRONICS	10.0	1	10.0
ELECTRONICS COVER	11.3	1	11.3
THERMAL ISOLATION TRUSS	8.0	1	8.0
QUICK DISCONNECTS	1.8	4	7.2
SUPER INSULATION	12.4	1	12.4
MISC. HARDWARE	10.0	1	10.0
TOTAL INSTRUMENT WEIGHT-LBS			219.2
TOTAL INSTRUMENT WEIGHT - KG			99.6

1.NOTE: Beryllium has a specific heat 2.03 times that of aluminum and thus may be used in certain areas to lighten the thermal heatsink and still maintain the desired temperature stability.

A preliminary power estimate for the ERA is given in Table 3.3.

TABLE 3.3
POWER ESTIMATE

	POLAR PLATFORM 85 DETECTORS
ELECTRONICS	80
MECHANISMS DRIVES	15
THERMAL CONTROL	20
TELEMETRY/LAN INTERFACES	15
TOTAL POWER (Watts)	130

4.0 DETECTOR AND ELECTRONICS DESIGN

4.1 DETECTOR EQUATION

The basic operation of the dual cavity detector is illustrated in Figure 4.1, which shows an idealized representation of the detector. A cutaway sketch of the detector is shown in Figure 4.2. Great care is taken in manufacturing the detectors to match primary side and reference side components to have the same thermal and electrical properties. The reference cone views a surface connected directly to the instrument heatsink. The primary side views the scene through an aperture which produces the desired field of view (FOV). The rest of the FOV of the primary side sees the baffle/heatsink material which is at the same temperature as the material seen by the reference cone.

The detector operates in a differential mode. Power is applied to the heater winding in the primary cone until the temperature drop across the primary thermal shunt (cylinder) equals the temperature drop across the reference thermal shunt. This is done by means of the bridge circuit shown in Figure 4.1b in which R_p and R_r represent the primary and reference temperature sensor windings. This differential method measures power directly without any conversion efficiency and makes the measurement independent of the absolute value of detector responsivity.

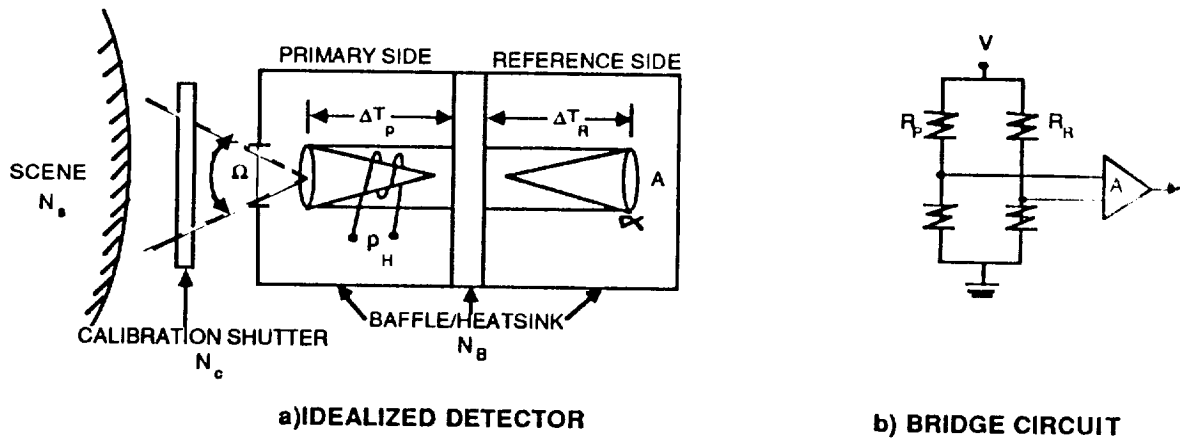


FIGURE 4.1. BASIC OPERATION FOR ACR DETECTOR

Equations one through four show the derivation of the basic measurement equation. Equation 1 states the basic principle that power is applied until the temperature drops across the primary and reference shunts are equal. Equation 2 shows the temperature drop as a product of thermal resistance and net power flow through the thermal impedance. Equation 3 includes the input and output power terms that produce the net power flow through the thermal impedance. Equation 3 shows the temperature balance equation as the scene is being measured. The scene radiance is represented by N_s .

During the calibration phase the equation is identical, with the exception that the radiance from the calibration shutter takes the place of the scene radiance. If a highly reflective shutter is utilized, the shutter radiance is replaced by the baffle/heatsink radiance, N_b . When these two equations are subtracted the final detector equation shown in Equation 4 is derived.

EQ.1: $\Delta T_p = \Delta T_r$

EQ. 2: $R_p \cdot (P_{inp} - P_{outp}) = R_r \cdot (P_{inr} - P_{outr})$

EQ. 3: $R_p [P_h + a \cdot N_s \cdot A \cdot \Omega + a \cdot N_b \cdot A \cdot (\pi - \Omega) - \Sigma P_{lp}] = R_r [a \cdot N_b \cdot A \cdot \pi - \Sigma P_{lr}]$
 $R_p [P_h + a \cdot N_b \cdot A \cdot \Omega + a \cdot N_b \cdot A \cdot (\pi - \Omega) - \Sigma P_{lp}] = R_r [a \cdot N_b \cdot A \cdot \pi - \Sigma P_{lr}]$

BASIC SCENE RADIANCE EQUATION

EQ. 4:
$$N_s = N_b - \frac{\Delta P_h}{a \cdot A \cdot \Omega} + \frac{(R_r \cdot \pi - \pi + 1) \cdot \Delta N_b}{R_p \cdot \Omega} + \frac{\Delta \Sigma P_{lp}}{a \cdot A \cdot \Omega}$$

Where:

- N_s = Scene radiance, effective inband ($W/cm^2 \cdot sr$)
- N_b = Baffle/Heatsink radiance, effective inband ($W/cm^2 \cdot sr$)
- ΔP_h = Δ in heater power between scene and calibration viewing (W)
- ΔN_b = Δ in effective inband Baffle/Heatsink radiance between scene and calibration viewing ($W/cm^2 \cdot sr$)
- $\Delta \Sigma P_{lp}$ = Δ in total stray power losses in primary cone between scene and calibration viewing ($W/cm^2 \cdot sr$)
- a = Cone absorptance
- A = Collecting area of cone (cm^2)
- Ω = FOV of cone (sr)
- R_r, R_p = Thermal resistance of reference and primary shunts

By examining the final detector equation several important facts can be seen:

1. Temperature gradients along the baffles do not matter as long as these gradients do not change between calibrations.
2. The absolute responsivity of the detector does not enter into the equation. It only effects the SNR because the bridge circuit is nulled no matter what the gain is. Only the ratio of the reference side to primary side thermal resistance enters into the equation, and only as a multiplier to the change in baffle radiance. On the first two detector units tested at SI, this ratio was within 2.7% of unity. This non-dependence on both gain and linearity is a key feature of this type of detector. It eliminates the need to balance the gains of the individual detectors that make up the array.
3. The absolute values of the stray power losses in both the primary and reference sides of the detector do not matter as they are subtracted out by differencing. Only the change in these losses between the scene and calibration measurements enters into the equation. The main difference in these values would be the amount of radiation lost through the aperture when it is viewing a scene and when it is

shuttered. (When the detector is operating in air during laboratory testing there will also be a change due to the difference in air convection currents when the shutter is opened or closed.) The other power losses such as through the electrical leads are constant and subtract out. Additionally, the absolute value of this difference in radiation loss between the scene and calibration measurements can be calculated theoretically and compensated for by knowing the scene and baffle radiances.

4. The third term in the equation, which is proportional to the change in heatsink/baffle radiance between calibrations, can theoretically be made as small as desired by increasing the thermal mass of the heatsink and/or calibrating more often. Calibrating more often is equivalent to operating in a chopped mode. The size of these thermal drifts between calibrations will be analyzed during the thermal modelling and analysis.
5. The absolute accuracy of the measurement depends on the knowledge of the absolute temperature and emissivity of the baffle/heatsink which produce N_b . If the scene produces a much higher radiance than the heatsink, such as in solar monitoring, this term can be considered negligible and the absolute radiance of the scene can be determined without measuring the heatsink parameters. In the case of earth observing, the scene and heatsink temperatures are similar and the heatsink temperature must be accurately monitored. The baffle/heatsink structure shall thus be accurately instrumented in all locations that can be viewed by the detector by means of reflection off of the calibration shutter. A 2nd option that could be employed is to use a shutter that contains a well calibrated blackbody, whose radiance can be accurately measured. The ERA is designed such that the shutter can contain a wide FOV inflight blackbody similar to those used on the ERBE instruments.
6. Equation 4 assumes negligible electronic drifts between calibrations. To insure that this is accomplished, the following adjustments are performed on each preamplifier during assembly:
 - a. Balance opamp offset to zero
 - b. Balance common mode offset to zero
 - c. Normalize sensor resistances and adjust bridge calibration point
 - d. Normalize heater resistance to produce desired dynamic range
7. When the changes in heatsink temperature and stray losses between calibrations are reduced to negligible values, the resulting accuracy of the scene measurements is limited only to the knowledge of a , A , and Ω and the ability to measure small changes in heater power, ΔP_h . By using specular black paint and a bent cone tip structure that eliminates any meniscus at the bottom, the absorptance of the cone is known to better than 0.1 %. To reduce the quantization error to less than 10% of the desired overall precision, 13 bits are required. To allow extra margin for future versions of the ERA, 16 bit encoding has been incorporated in the design.

4.2 DETECTOR MODULE DESIGN

Because of the large number of detectors required in the array, an integrated detector/preamplifier module concept has been developed by Space Instruments. The module contains the detector, limiting aperture, thermal reference cap, and the preamplifier electronics. The instrument is designed so that the Field of View defining apertures are part of the overall instrument heatsink. This allows each detector module to be interchangeable with any other. This greatly simplifies detector testing and selection and instrument assembly. By including the preamplifier as part of the module the low level detector signals are contained within the module. This reduces the problems of noise interference which are inherent in a design where the electronics are distributed due to the physical layout of the instrument. A cutaway view of the detector (courtesy of JPL) without the module is shown in Figure 4.2.

An exploded view of the detector module is shown in Figure 4.3. The sections of the figure show the order in which the detector module is assembled. The detector, front baffle tube, rear thermal cap and wire cover all mount directly to the copper mounting flange. This flange mounts directly to the instrument heatsink. The final detector module becomes a ruggedized unit. For the breadboard hardware, the parts (except for the flange) were machined from aluminum and black anodized. To provide a better thermal path to the instrument heatsink, the front baffle tube and rear thermal cap can be machined from copper.

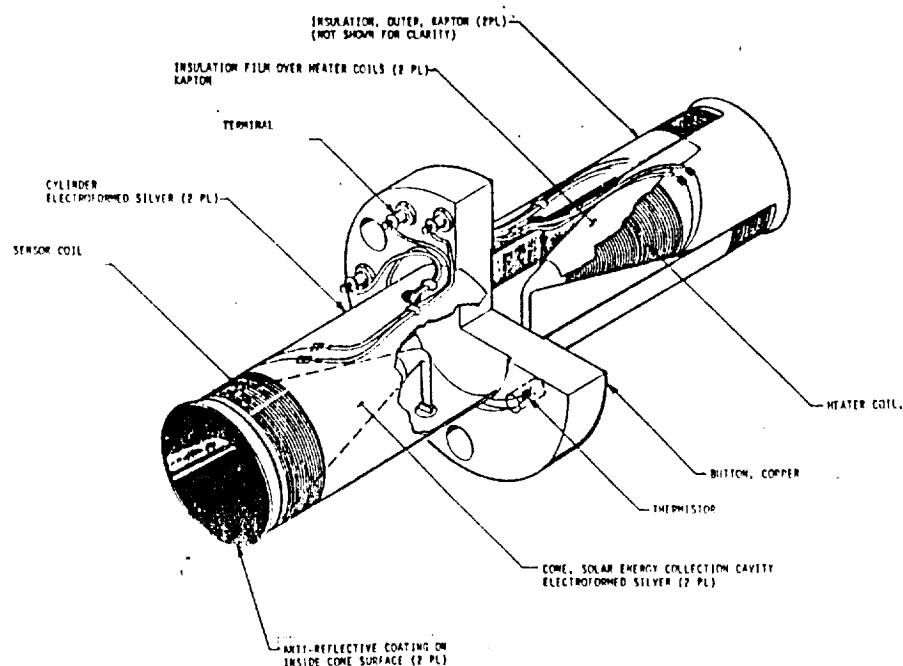


FIGURE 4.2. ACR DETECTOR

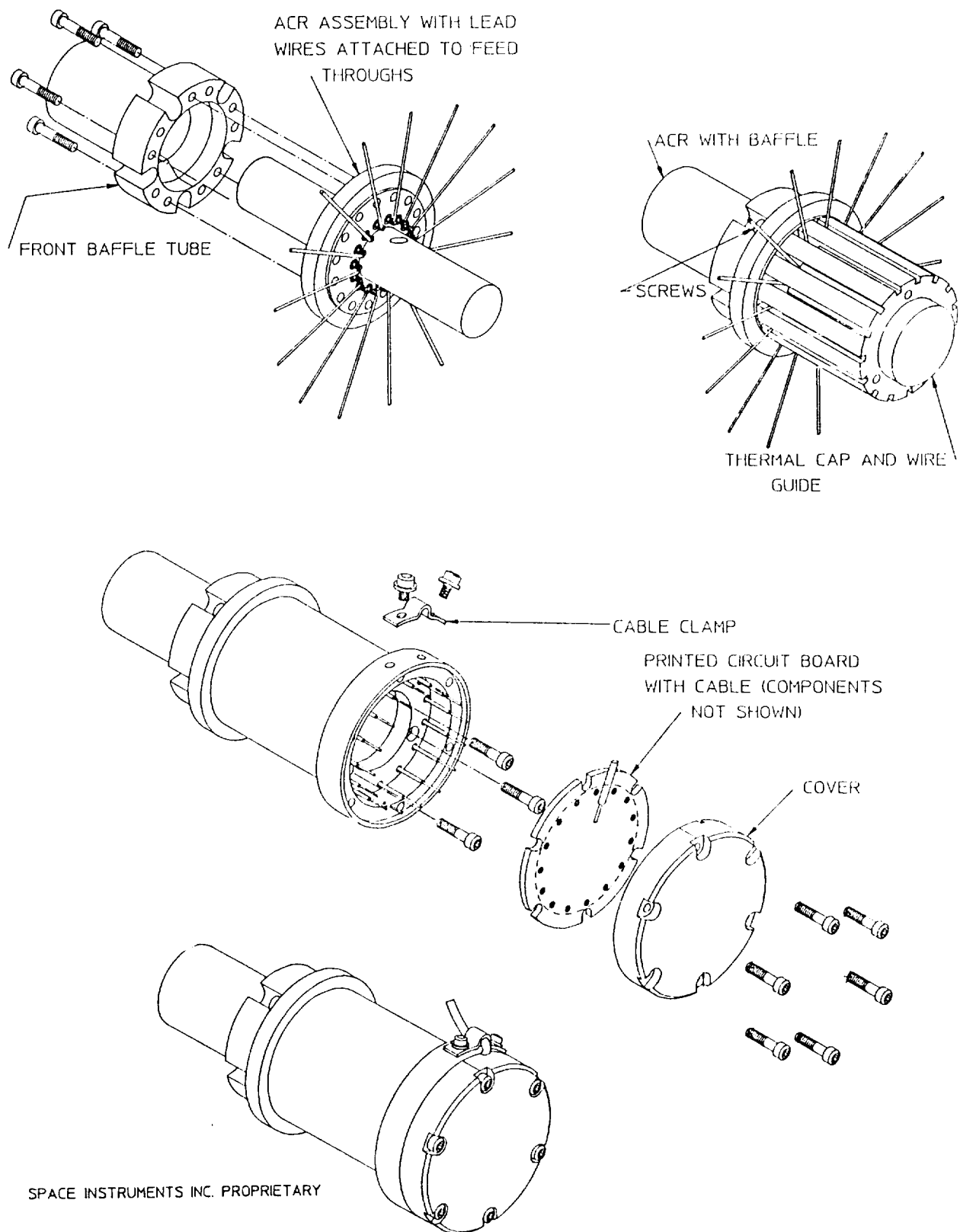


FIGURE 4.3. DETECTOR MODULE - EXPLODED VIEW

4.3 ELECTRONICS DESIGN

An overall block diagram for the detector, electronics and the breadboard development system is shown in Figure 4.4. The bridge and preamplifier circuits are located on the circuit board within the detector module. The high level signal output of the preamp is then routed to the electronics unit which is located separately. The low pass filter is a single stage filter which eliminates the high frequency components which would otherwise cause aliasing after sampling. The output from the filter then goes to a sample/hold and an analog multiplexer. The multiplexed signals are then routed to a single A/D converter. The resulting digital signal is input to the microprocessor.

The microprocessor implements the control loop compensation filter in software and, at the correct time for each detector, outputs the digital command to the correct DAC for that detector. The digital filter compensates for the thermal time constants of the detector and provides the desired settling time, damping ratio, and phase margin at the selected sampling frequency. This is important because the detector has a transfer function containing three poles with time constants of approximately 8.0, 0.8 and 0.2 seconds. These poles must be compensated for to provide the required overall closed loop time constant and settling time.

The DAC provides the voltage command to the power drive circuit for the heater element located on the primary cone of the detector. For the breadboard system, a Motorola 68,000 microprocessor was selected. This enabled a Mac II computer to be used as a software development system. A timing study showed that a single 68000 has sufficient speed to handle an array of up to 1000 detectors.

When operating in the development mode, the microprocessor acts as a communication device to pass the error voltage from the detector to the Mac II computer. The signal is routed through an SCC and an RS422 terminal into the Mac II. The compensation filter is then implemented in software in the Mac II. The resulting heater command is then transmitted back through the SCC to the DAC and fed to the heater.

The Mac II computer can also be used for a download mode in which software can be downloaded from the computer into RAM residing in the electronics unit. The system can then be operated internally from this downloaded software. To run the breadboard system in a completely stand alone mode a nominal set of software is stored in E-PROM located within the electronics unit. This internal software also operates the test fixture heater control loop. The functions of the software packages will be described in Section 7.0.

The remaining electronics consists of health and status (housekeeping), mechanism drives, thermal control, power supplies, and timing. Housekeeping in the flight instrument will include temperatures at various locations on the instrument, power supply voltages, and operating mode information. The mechanism drive electronics will operate the shutters, spectral filter, and contamination cover. The thermal control

electronics will power heaters which in conjunction with passive radiators will provide instrument heatsink temperature control. The power supplies will convert the platform AC into the required power forms. The preliminary voltages are +5 VDC, +15 VDC, -15 VDC, +24 VDC, and +45 VDC.

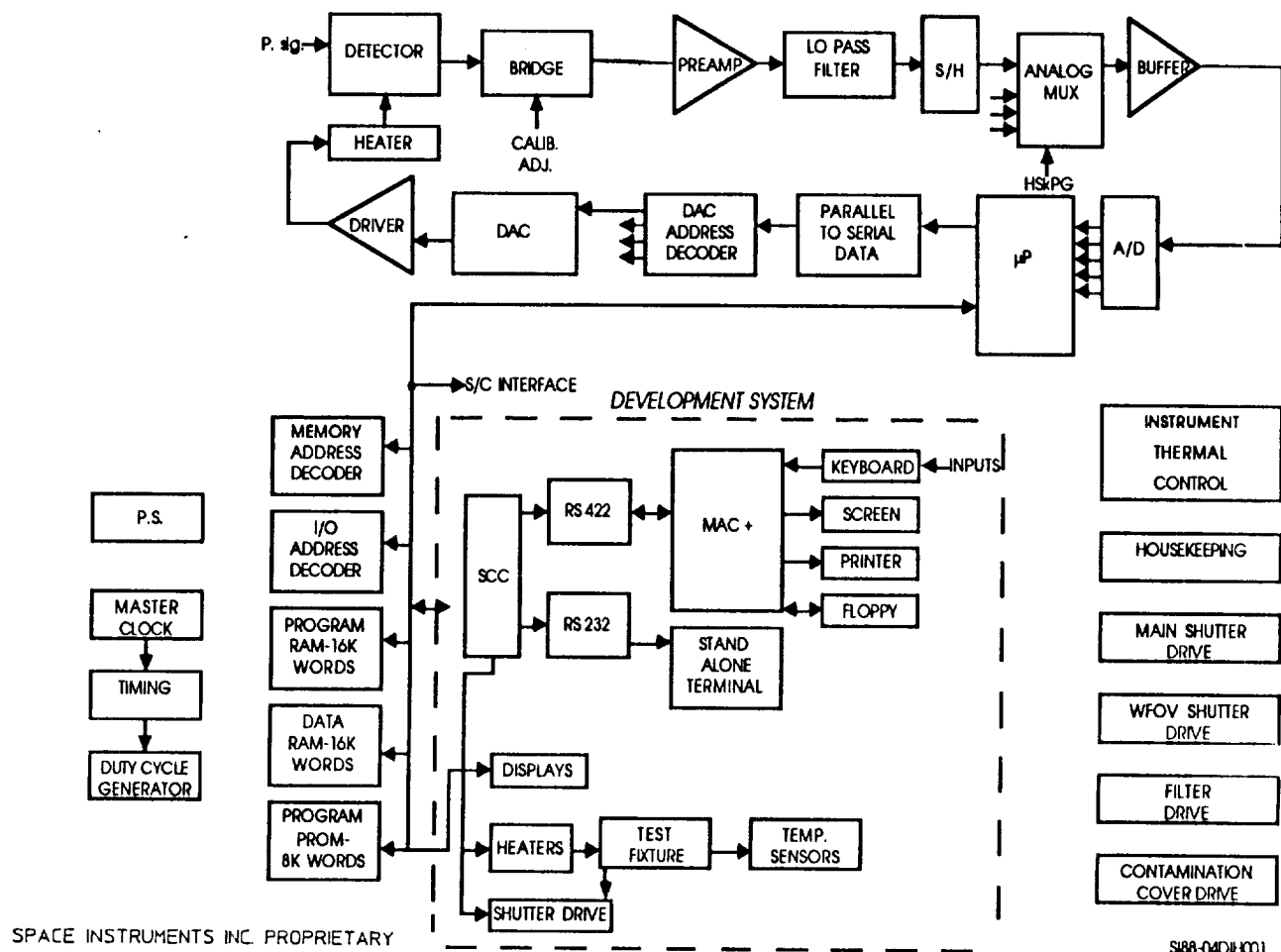


FIGURE 4.4. ELECTRONICS AND DEVELOPMENT SYSTEM BLOCK DIAGRAM

4.4 CONTROL LOOP ANALYSIS

A computer simulation was utilized to predict how the closed loop system would perform when different digital compensation filters were employed. Two different filters were analyzed; an IIR and a R filter containing gain, integration, first difference and second difference terms. Open and closed loop frequency responses were plotted along with step input dynamic responses. As the breadboard hardware is tested by inserting a step input of radiance via the shutter and blackbody, the step input provides the best means of comparison with actual hardware results.

Figure 4.5 shows the theoretical step response of the loop utilizing the IIR filter. The figure shows a large single overshoot in the output signal. Figure 4.6 shows the error signal response to the same step input. The settling time is on the order of 14 seconds. The error signal provides a better method of measuring the response as it must always come back to zero when the loop is operating correctly.

Figure 4.7 shows the step response to the same input after one of the gain terms has been decreased from 23.531 to 23.344. The resulting error signal for this new IIR filter is shown in Figure 4.8. It can be seen that even this slight change in one of the filter parameters produces a different response function which now has four overshoots and a settling time on the order of 19 seconds. This extreme sensitivity to the IIR filter parameters was confirmed with the breadboard hardware. The majority of tests during system integration testing were run with the R filter which exhibited greater stability and was more easily optimized for the desired time response. Examples of loop response using this filter are given in Section 8.0.

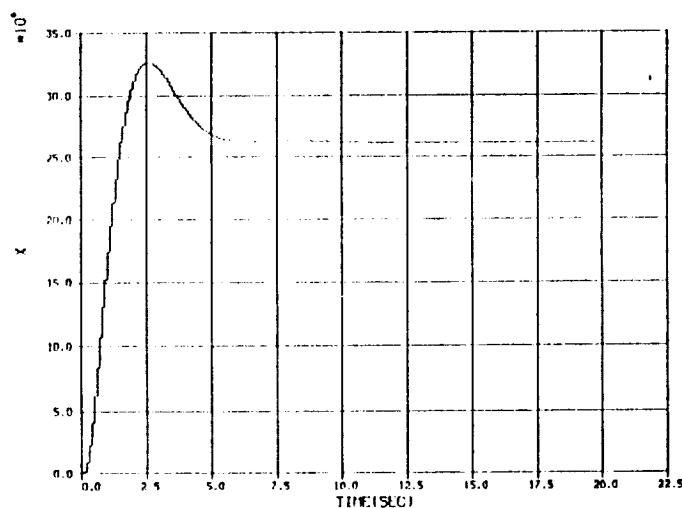


FIGURE 4.5. THEORETICAL STEP RESPONSE OUTPUT WITH IIR FILTER, A=23.344

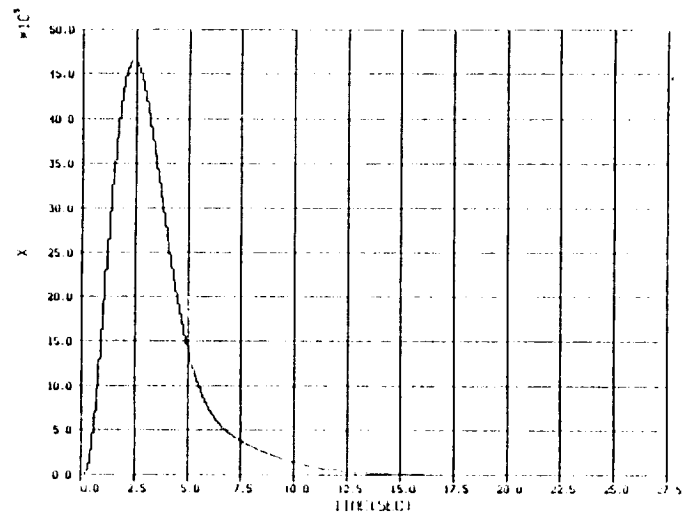


FIGURE 4.6. THEORETICAL STEP RESPONSE ERROR WITH IIR FILTER, A=23.344

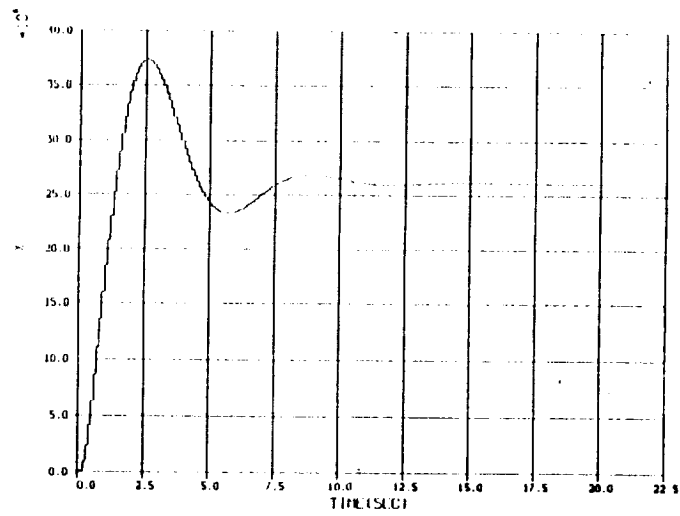


FIGURE 4.7. THEORETICAL OUTPUT WITH IIR FILTER, A=23.531

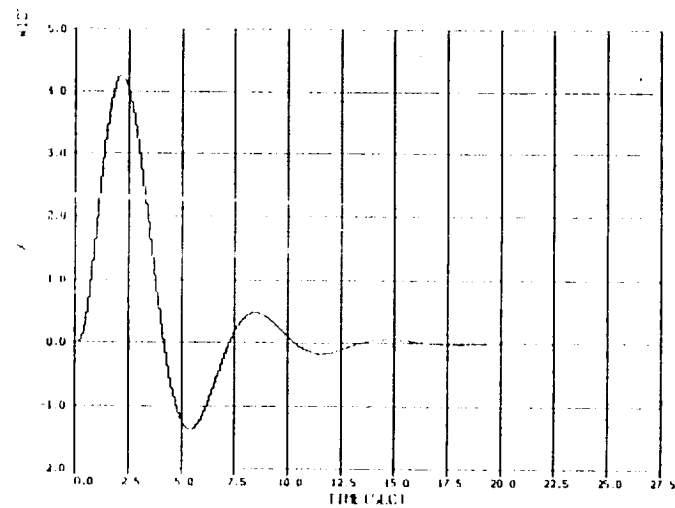


FIGURE 4.8. THEORETICAL ERROR WITH IIR FILTER, A=23.531

5.0 RADCON COMPUTER SIMULATION

5.1 RADCON PROGRAM DESCRIPTION

In order to design the ERA instrument a computer simulation was developed by SI. This computer simulation is called RADCON for Radiometric Configuration. With RADCON any desired pattern can be constructed at the Top Of the Atmosphere (TOA). Once the pattern and orbital parameters are inserted, the instrument parameters are calculated and RADCON produces graphical outputs showing the footprint pattern at TOA and the exact shape and size of each field aperture for a planar configuration. It also gives the exact location and LOS angle for each detector and computes the exact power incident on each detector in order to calculate the precision. In addition, RADCON calculates the IFOV and the wing energy ratio for that detector. A list of inputs and outputs for the RADCON program is summarized in Table 5.1.

TABLE 5.1

RADCON COMPUTER SIMULATION

INPUTS:

- ORBIT PARAMETERS
- NUMBER OF PIXELS/RING
- FOOTPRINT AREA (SPATIAL RESOLUTION)/PIXEL
- DESIRED ASPECT RATIO
- BAFFLE LENGTH AND COMMON APERTURE SEPARATION

OUTPUTS:

GRAPHICAL:

- FOOTPRINT PATTERN AT TOA
- FIELD APERTURE SHAPES
- DETECTOR PATTERN

QUANTITATIVE:

- INSTRUMENT DESIGN PARAMETERS
- EARTH PATTERN PARAMETERS
- POWER INPUT TO EACH DETECTOR
- WING ENERGY FOR EACH DETECTOR
- IFOV FOR EACH DETECTOR FIELD APERTURE
- CONICS

Figure 5.1 shows the earth/spacecraft geometry used in RADCON and Figure 5.2 shows the instrument layout geometry. Two sample outputs from the RADCON program are illustrated in Figure 5.3. On the left the number of pixels has been input for each ring along with the desired area for each pixel. The program then calculates the shape of each pixel and the resultant aspect ratio. It can be seen that these range from 0.67 to 1.39.

On the right side the unity aspect ratio option is exercised. In this option, a pattern is produced that has the same number of detectors (85) but RADCON optimizes the number of pixels in each ring to produce aspect ratios close to 1.0. The resultant aspect ratios lie between 0.98 and 1.03 for this example. To match up successive ground areas from different orbits this is the preferred method.

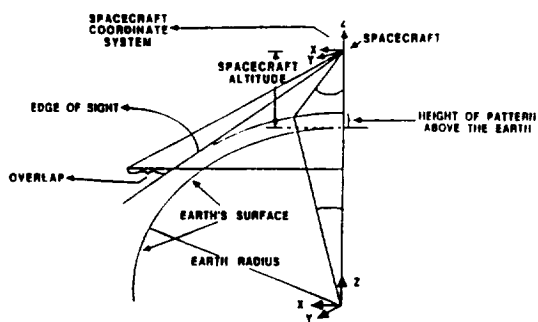


FIGURE 5.1. EARTH-SPACECRAFT GEOMETRY

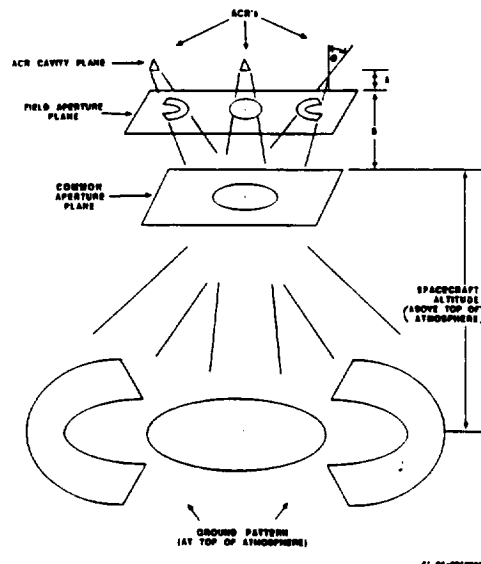
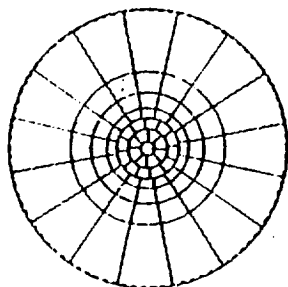


FIGURE 5.2. FIELD APERTURE GEOMETRY

RADIAL PATTERN - 85 DETECTORS

(ALL PIXELS IN A LINE)



ASPECT RATIO - RADIAL

1.00
0.78
1.25
1.39
1.26
1.19
0.67

RING NO.

0
1
2
3
4
5
6

ASPECT RATIO - EQUAL

0.00
0.99
0.98
1.00
1.02
1.01
1.03

EQUAL ASPECT PATTERN - 85 DETECTORS

(GROUND PIXEL ASPECT RATIO = 1.0)

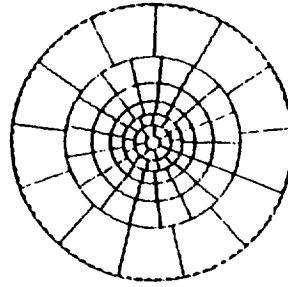


FIGURE 5.3. RADCON EARTH PATTERN OUTPUTS

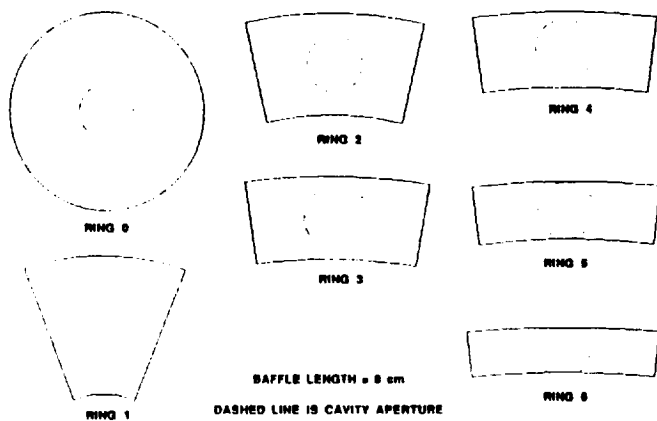


FIGURE 5.4. FIELD APERTURE SHAPES

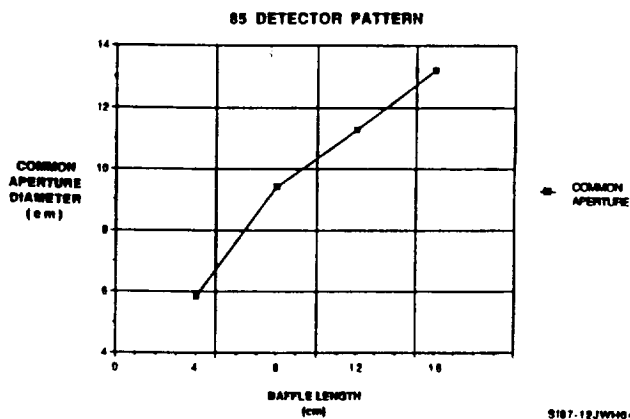


FIGURE 5.5. COMMON APERTURE VRS. BAFFLE LENGTH

Once a ground pattern has been selected RADCON calculates the exact field aperture shapes, and sizes for a planar configuration and gives the exact conic parameters plus a graphical output. An example of this is shown in Figure 5.4 RADCON also computes the size of the common aperture. Figure 5.5 shows a trade off in which this common aperture diameter is plotted as a function of baffle length. As the baffle length increases, the wing energy ratio is reduced but the common aperture diameter increases, thus increasing the shutter and filter sizes and the overall instrument size.

A tradeoff of wing energy versus baffle length is shown in Figure 5.6. Because of the statistical integrating of measurements taken on different orbits over a long period of time it is not critical to reduce this wing energy ratio to a very small number. For instance, if the footprint pattern at some angle was square and was combined with a circular nadir footprint that was perfectly registered and just fell within the square, the area mismatch would be 21%. Therefore, it is not necessary to reduce the wing energy to below this approximate value.

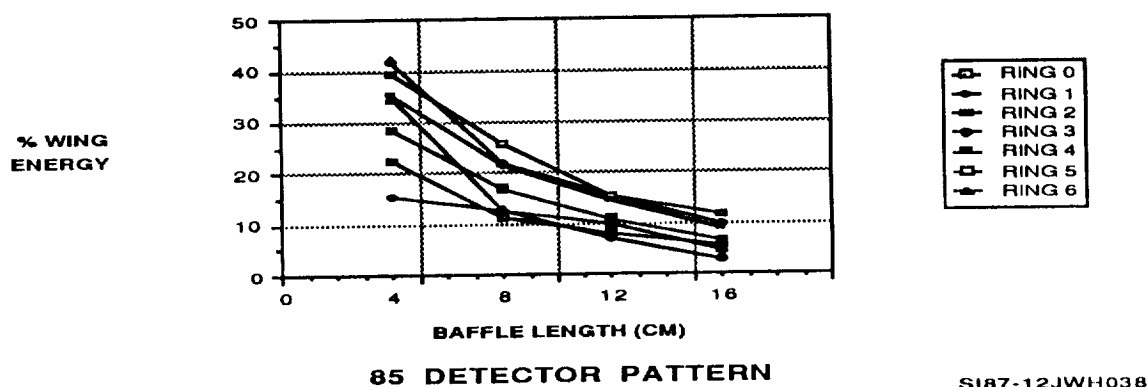


FIGURE 5.6. WING ENERGY VRS. BAFFLE LENGTH

5.2 RADCON SAMPLE RUN

Table 5.2 shows a sample run for from the RADCON program. The run assumes a spacecraft altitude of 833 Km such as that used on typical polar orbit satellites. Tables 1 and 2 give the details of the pattern produced at the TOA. Table 3 gives the total input power into each detector and the percent of that power that comes from outside the footprint-eg. % wing energy. Table 4 gives the IFOV of each detector and the power recieved from the footprint area only. Table 5 gives the wing power values. Tables 7 and 8 give the exact dimensions and shapes of each of the field apertures for a planar configuration. The RADCON program was used a great deal in the early design stages of the ERA. Many tradeoff studies were performed and the baseline configuration with a baffle length of approximately 8 cm and a central opening of approximately 9.4 cm was derived.

TABLE 5.2. SAMPLE RUN

HEIGHT OF PATTERN ABOVE EARTH = 50.00 KM
 COVERAGE SURFACE OVERLAP = 25.00 KM
 SPACECRAFT ALTITUDE = 833.00 KM

TABLE 1. GROUND PATTERN OUTLINE PARAMETERS

CIRCLE NO.	CHORD RADIUS (KM)	ARC- RADIUS (KM)	CIRCUM- FERENCE (KM)
1	141.04	141.05	886.18
2	422.91	423.22	2657.25
3	645.54	646.63	4056.07
4	856.05	858.60	5378.69
5	1166.75	1173.26	7330.92
6	1613.56	1631.01	10138.32
EDGE OF SIGHT	2913.08	3023.32	18303.43
7	2938.08		18460.51

TABLE 2. GROUND PATTERN DETAIL PARAMETERS

RING NO.	NO. OF SUB- REGIONS IN RING	EDGE LENGTH OF SUB- REGION (KM)	INNER ARC- LENGTH OF SUB- REGION (KM)	OUTER ARC- LENGTH OF SUB- REGION (KM)	AREA OF SUB- REGION (SQR KM)	SQUARE ROOT OF SUB- REGION AREA (KM)	OVERLAP PARAMETER (KM)
0	1	141.05	0.00	886.18	6.2500E+04	250.00	0.00000
1	8	282.17	110.77	332.16	6.2500E+04	250.00	0.78505
2	12	223.41	221.44	338.01	6.2500E+04	250.00	1.25223
3	16	211.96	253.50	336.17	6.2500E+04	250.00	1.39117
4	16	314.66	336.17	458.18	1.2500E+05	353.55	1.26262
5	16	457.75	458.18	633.65	2.5000E+05	500.00	1.19335
6	16	1392.31	633.65	1143.96	1.2424E+06	1114.61	0.67475
OVERLAP	16	25.00	1143.96	1153.78	2.8722E+04	169.48	INC'D ABOVE

TOTAL NUMBER OF DETECTORS REQUIRED = 65
 INTEGRATION RESOLUTION PARAMETER N = 8

TABLE 3. TOTAL POWER INPUT

SUB- REGION IN RING NUMBER	EFF. SOLID ANGLE FROM FOOTPRINT AND WING (sr)	EFF. COLL. AREA FROM FOOTPRINT AND WING (m ²)	POWER INPUT FROM FOOTPRINT AND WING (m ² *sr)	PERCENT WING POWER (%)
0	1.58430E-01	3.07152E-05	4.94067E-06	11.26
1	1.29191E-01	2.91721E-05	3.92995E-06	12.66
2	9.39760E-02	2.75462E-05	2.61750E-06	16.93
3	6.42299E-02	2.48604E-05	1.62469E-06	21.52
4	7.95905E-02	2.28301E-05	1.84162E-06	21.30
5	7.68396E-02	1.98769E-05	1.63934E-06	25.41
6	3.73080E-02	3.31912E-05	1.18429E-06	12.63

TABLE 5.2 CONT.

TABLE 4. FOOTPRINT POWER INPUT

SUB- REGION IN RING NUMBER	EFF. SOLID ANGLE FROM FOOTPRINT (sr)	EFF. COLL. AREA FROM FOOTPRINT (m ²)	MAXIMUM POSSIBLE POWER FROM FOOTPRINT (m ² *sr)	ACTUAL POWER RECEIVED FROM FOOTPRINT (m ² *sr)
0	9.91890E-02	4.40817E-05	4.94726E-06	4.38417E-06
1	7.92927E-02	4.30499E-05	3.95877E-06	3.43254E-06
2	5.19820E-02	4.17674E-05	2.60060E-06	2.17432E-06
3	3.28243E-02	3.87257E-05	1.64424E-06	1.27514E-06
4	3.69491E-02	3.90595E-05	1.84940E-06	1.44929E-06
5	3.29317E-02	3.69417E-05	1.64752E-06	1.22283E-06
6	2.71494E-02	3.54707E-05	1.35808E-06	1.03236E-06

TABLE 5. WING POWER INPUT

SUB- REGION IN RING NUMBER	EFF. SOLID ANGLE FROM WING AREA (sr)	EFF. COLL. AREA FROM WING AREA (m ²)	INPUT POWER FROM WING AREA (m ² *sr)
0	5.92408E-02	9.32887E-06	5.56493E-07
1	4.98988E-02	9.57988E-06	4.97407E-07
2	4.19940E-02	1.04808E-05	4.43173E-07
3	3.14056E-02	1.09951E-05	3.49557E-07
4	4.26414E-02	9.39882E-06	3.92329E-07
5	4.39079E-02	9.09908E-06	4.16507E-07
6	1.01586E-02	1.49553E-05	1.51924E-07

TABLE 6. TOTAL RING POWER INPUT

RING NO.	MAXIMUM POSSIBLE POWER FROM RING (m ² *sr)	ACTUAL POWER RECEIVED FROM RING (m ² *sr)	WING POWER RECEIVED FROM OUT- SIDE RING (m ² *sr)	TOTAL POWER RECEIVED (m ² *sr)	PERCENT WING POWER (%)
0	4.94726E-06	4.38417E-06	5.56493E-07	4.94067E-06	11.26
1	3.16702E-05	2.74603E-05	3.97926E-06	3.14396E-05	12.66
2	3.12072E-05	2.60919E-05	5.31808E-06	3.14099E-05	16.93
3	2.63078E-05	2.04022E-05	5.59291E-06	2.59951E-05	21.52
4	2.95904E-05	2.31887E-05	6.27727E-06	2.94659E-05	21.30
5	2.63604E-05	1.95653E-05	6.66412E-06	2.62294E-05	25.41
6	2.17293E-05	1.65178E-05	2.43079E-06	1.89486E-05	12.83
TOTAL	1.71813E-04	1.37610E-04	3.08189E-05	1.68429E-04	18.30

TABLE 7. APERTURE PARAMETERS

RING NO.	DETECTOR POINTING ANGLE (DEG)	CAVITY-FIELD APERTURE SEPARATION (CM)	FIELD-COMMN. APERTURE SEPARATION (CM)	CENTER WIDTH (CM)	ARC LENGTH (CM)	ASPECT RATIO
0	90.00	8.00	12.00	1.4382	0.0000	0.0000
1	70.93	8.00	12.00	2.5002	2.0642	0.8256
2	58.64	8.00	12.00	1.4576	2.3068	1.5825
3	48.05	8.00	12.00	1.0022	2.1122	2.1075
4	40.90	8.00	12.00	0.9978	2.3922	2.3974
5	34.42	8.00	12.00	0.8146	2.6146	3.2097
6	29.13	8.00	12.00	0.6635	2.7715	4.1769

DIAMETER (CM) OF COMMN. APERTURE = 9.423

TABLE 8. DETAIL APERTURE PARAMETERS (CONICS)

RING NO.	UPPER EDGE ECCEN-TRICITY	UPPER EDGE FOCUS (CM)	LOWER EDGE ECCEN-TRICITY	LOWER EDGE FOCUS (CM)
1	3.69930E-01	1.81952E+00	3.32006E-01	5.36635E-01
2	6.97603E-01	8.60572E+00	6.19220E-01	4.26373E+00
3	9.54283E-01	8.70527E+01	8.52561E-01	1.97666E+01
4	1.24650E+00	-2.36133E+01	1.07906E+00	-5.35064E+01
5	1.57866E+00	-1.38071E+01	1.36044E+00	-1.67743E+01
6	1.54074E+00	-1.11339E+01	1.67185E+00	-1.21583E+01

WHEN EXTENDED, APERTURE SIDES MEET A DISTANCE D FROM THE APERTURE CENTER FORMING AN ANGLE PHI.

RING NO.	D (CM)	PHI (DEG)
1	2.76598E+00	42.7582
2	5.22698E+00	25.2859
3	7.19037E+00	16.8305
4	9.23607E+00	14.8399
5	1.16771E+01	12.8287
6	1.43580E+01	11.0599

CENTER DETECTOR APERTURE RADIUS (CM) = 1.43818E+00

6.0 HARDWARE FABRICATION

Figure 6.1 shows photographs taken during the fabrication of the dual cavity detectors. Figure 6.1a shows the heater winding junction on the silver cavity as viewed through a microscope. Figure 6.1b shows the completed detector cavities after winding and application of the Kapton cover. Figure 6.1c shows the temperature sensor being wound about the end of the silver thermal shunt. A thin layer of epoxy is applied to the shunt and the temperature sensor wire wound into the epoxy while it is still soft. Figure 6.1d shows the completed dual cavity detectors with their copper mounting flanges. The detector module parts are then attached to the copper mounting flange.

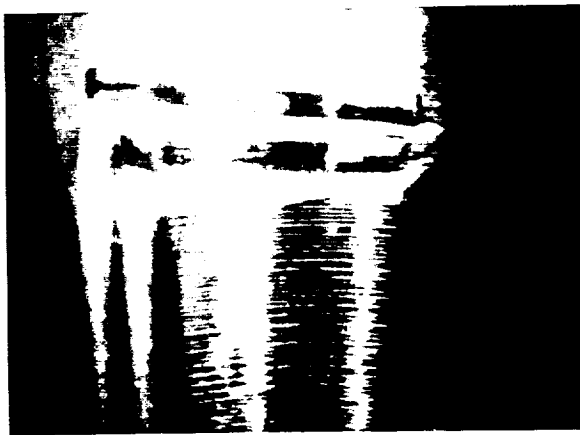


FIGURE 6.1a. CAVITY HEATER WINDING JUNCTIONS

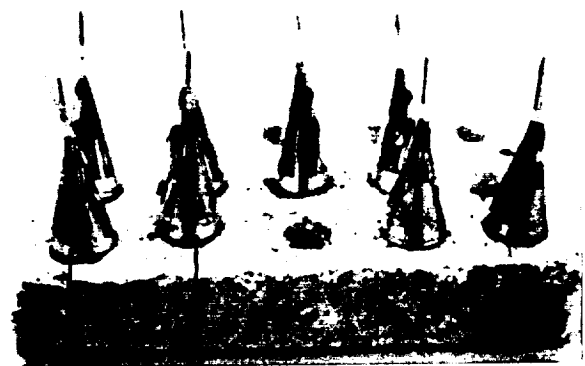


FIGURE 6.1b. DETECTOR CAVITIES AFTER WINDING

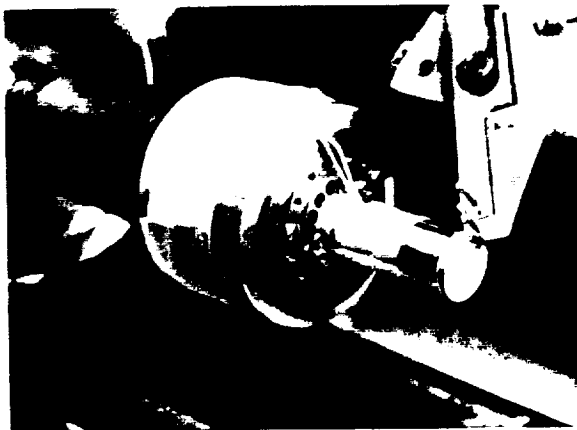


FIGURE 6.1c. TEMPERATURE SENSOR WINDING



FIGURE 6.1d. COMPLETE DUAL CAVITY DETECTORS

FIGURE 6.1 DUAL CAVITY DETECTOR FABRICATION

A photograph of a completed detector module is shown in Figure 6.2.

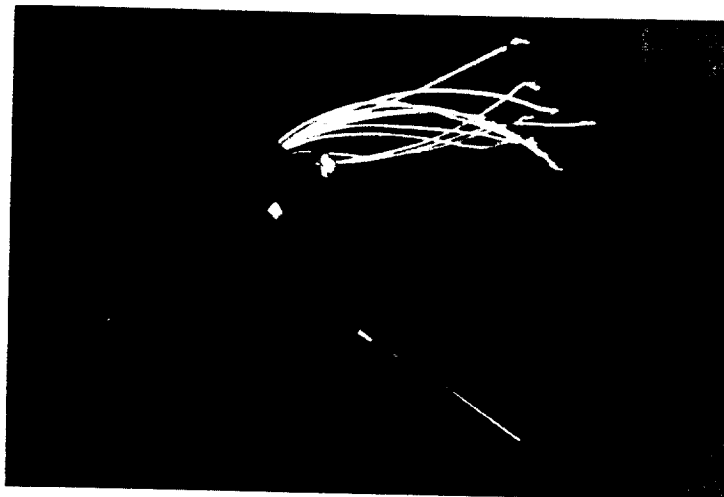


FIGURE 6.2. DETECTOR MODULE

A photograph of the completed electronics unit is shown in Figure 6.3. The electronics unit accepts up to three detector inputs. The unit operates either internally from software stored in E-PROM or externally from signals received from the Mac II development computer. An LED display is used to read out the heatsink and shutter temperatures and while running in a stand alone mode, the output of each detector in mW. While in the stand alone mode, a switch on the panel is used to open and close the shutter.

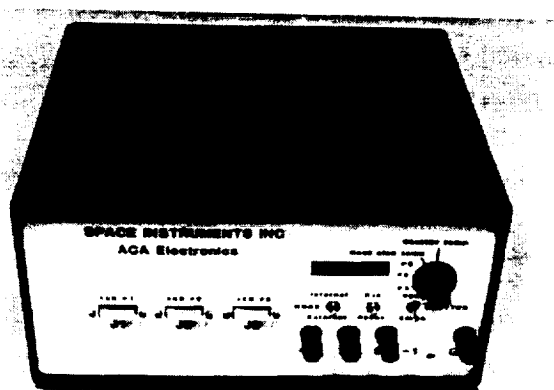


FIGURE 6.3. ELECTRONICS UNIT

7.0 SOFTWARE DEVELOPMENT

7.1 FILTER PROGRAM

The FILTER program was the most extensive software package developed for the project. It was the main development tool used to run system level tests with various digital filters and to process the resulting data. It provided the means to control the system parameters during testing and to display the data in real time on the MAC II monitor. It also sends the commands to open and close the calibration shutter.

Figure 7.1 shows a typical monitor display during a step input test. This copy of the realtime image was obtained via a screen dump to the dot matrix printer. The test utilized an IIR filter with the parameters given at the top of the display. The "Real" designation on the top line shows that every data sample is being displayed. The program can also average or smooth as many points as desired for long duration tests.

The top trace shows the detector output response to 2 step functions of radiance as the shutter is opened to view the blackbody and then closed. The display can be changed to display the integrator output instead, if desired. The bottom trace shows the error signal which goes negative, to decrease the heater power when the blackbody is viewed, and then returns to zero after a single overshoot. Each tick mark on the time axis is approximately 0.8 seconds.

Displayed at the top of the screen are the digital values for the error signal, output count level, and mounting flange temperature respectively for each of the three detectors. Also shown are the same parameters for the loop controlling the temperature of the large aluminum heatsink block to which the detectors are mounted. The number of data points collected is also displayed, when the S key is depressed to begin saving data. Any number of data points can be saved and dumped directly into the Cricket graphing program by merely depressing the D key. The mean, sigma, and standard deviation of each set of points saved is automatically computed and recorded.

The type of filter can be selected from the keyboard and the filter parameters changed in real time. This is one of the primary uses of the program. It allows iteration on filter parameters in real time without stopping operation. Other options are also available to initialize the screen, change the scale factors on the screen, adjust the heatsink temperature, and introduce offset biases.

Any amount of positive or negative bias can be inserted into the loop to make the detector stabilize at a new power level in order to measure closed loop responsivity. The FILTER program also includes the ability to introduce a ramp function with any desired amplitude and slope. This simulates actual radiance gradients produced as the instrument moves over the earth.

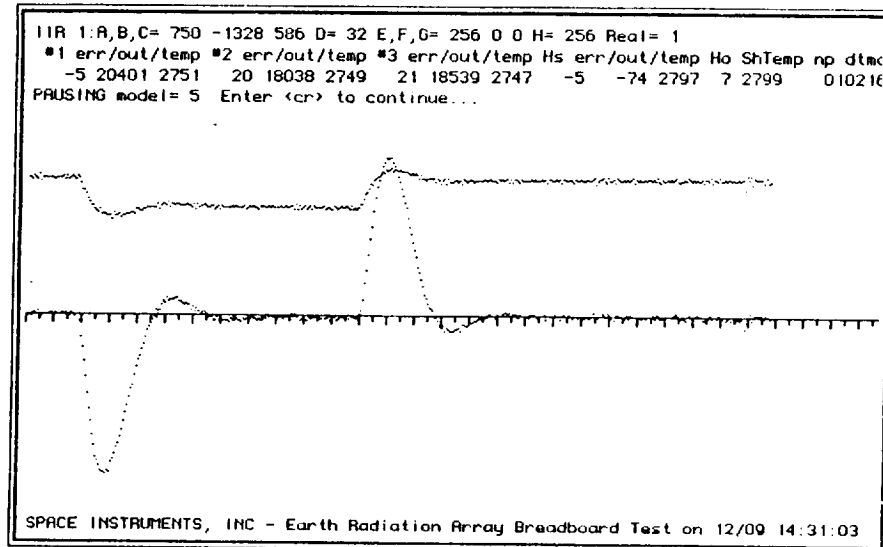


FIGURE 7.1. REAL TIME DISPLAY OF STEP INPUT RESPONSE WITH IIR FILTER

7.2 CAPCOMM.ASM PROGRAM

CAPCOMM.ASM is the communications software program which is downloaded to RAM in the digital control electronics. It provides for data transfer to and from the Mac II computer system. If the system is running on internal and the Mac II is not operating, the CAPCOMM.ASM program performs the heatsink and detector cap temperature control functions. During Mac II operation the CAPCOMM.ASM program sends detector error signals and PRT temperatures to the Mac II and receives detector heater commands, display values, shutter control signals, and temperature set levels from the Mac II.

7.3 TARGET.ASM PROGRAM

TARGET.ASM is the control electronics PROM based software. It allows stand alone operation in the internal mode or, in the external mode, allows software to be downloaded into RAM and executed.

In the stand alone mode, TARGET.ASM performs the control function on all three detectors and displays the average heater power in milliwatts. It also performs the heatsink temperature control function, displays heatsink and shutter temperatures in degrees C, and controls the shutter position in response to the front panel switch. In this internal mode, it simulates the way the instrument would perform while on orbit.

8.0 SYSTEM TESTING AND CHARACTERIZATION

8.1 TEST CONFIGURATION

A photograph of the laboratory test configuration is shown in Figure 8.1. The digital electronics unit is shown on the right. The test fixture, with three detectors mounted in it, is shown to the left of it. The three detectors are secured to the back of a large aluminum heatsink via servo clamps. A stepper motor is used to open and close the shutter wheel. The shutter is highly reflective on both sides to enable self calibration of the detectors and also to minimize heatloading from the blackbodies to the detectors. A heat shield is located in front of the shutter blade to prevent excess heat from the blackbody entering the detectors. Circular apertures are screwed into the heatsink to set the field of view to the desired value for each detector.

The blackbody is shown aligned with the topmost detector. The blackbody temperature controller is shown at left. The digital electronics unit has the ability to operate in the either the external mode through the development computer or in the self contained internal mode. In the external mode, the error signals from the detector are passed through the μ processor to the computer which contains the digital filter algorithms. The correct value is computed in the Mac II and sent back to the detector. In the internal or stand alone mode, all software is contained in internal E-PROM located within the electronics unit. In the internal mode, the power output reading of each detector in mW can be monitored via the LED display along with the heatsink and shutter temperatures. The front panel also contains a switch to manually open and close the shutter when operating in the internal mode.

The heatsink is controlled to a preset temperature and maintained to an accuracy of $\pm 0.005^\circ \text{C}$. While operating in the external mode this temperature can be set via the Mac II keyboard. The temperature is controlled by means of a digital control loop that has the same transfer function format as the detector control loop. The servo parameters and time response of this heatsink control loop can thus be adjusted from the keyboard. While operating in the internal or stand alone mode, the heatsink is normally controlled to 28°C . This produces a nominal operating level that approximates the nominal operating point that would be measured on orbit. During testing, a cover is placed over the rear portion of the detectors and the entire test fixture is enclosed in a styrofoam housing to minimize convection currents.

The blackbody used for calibration contains a deep grooved black anodized circular element with a PRT readout accurate to 0.005°C . The blackbody can be controlled to any temperature from 50 to 250°C . The temperature can be accurately monitored by means of a digital multimeter.

A large number of performance and characterization tests were run with the breadboard hardware. A short summary of the test program with one example of each type of test is presented in the following sections.

ORIGINAL PAGE
BLACK AND WHITE PHOTOGRAPH

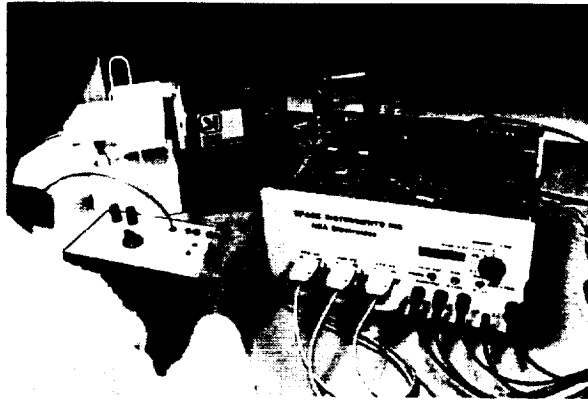


FIGURE 8.1. TEST CONFIGURATION

8.2. DETECTOR CHARACTERIZATION

8.2.1 OPEN LOOP DETECTOR RESPONSIVITY AND TIME CONSTANT

As each detector was manufactured, its responsivity and time constant were measured in an open loop mode. Figure 8.2 shows the results for detector no. 1. In this open loop test a step input of $20 \mu\text{W}$ is applied to the heater and the resultant decrease in output voltage is plotted. The final change in voltage divided by the step input of power is the responsivity. The time to reach 63% of the final value is the detector time constant. For detector no. 1 the responsivity measured 1.94 V/W and the time constant was 8.05 seconds. Using the measured physical parameters of the detector, the calculated responsivity was 1.58 V/W and the calculated time constant was 4.7 seconds.

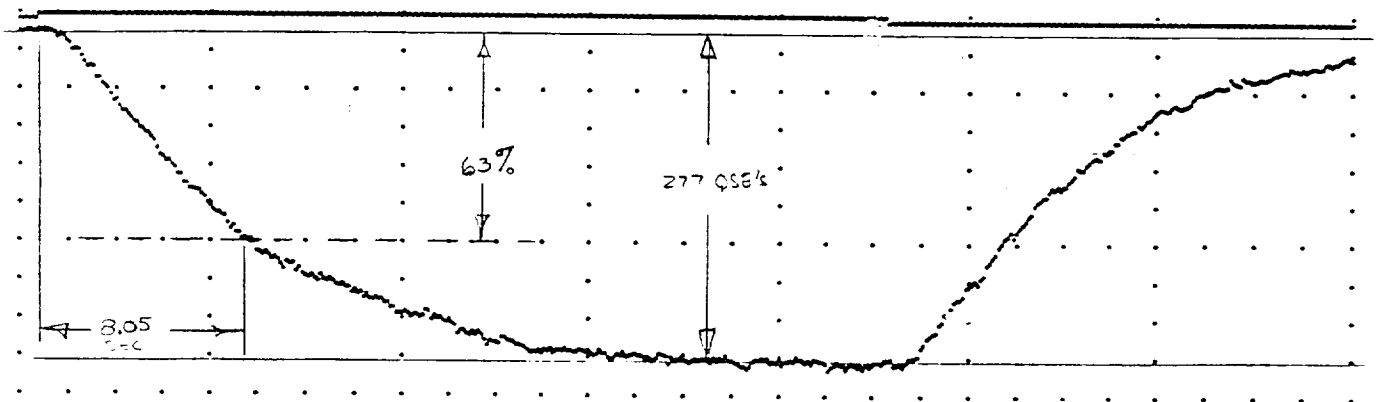


FIGURE 8.2

RESPONSIVITY AND TIME CONSTANT MEASUREMENT
DETECTOR 1

8.2.2 CLOSED LOOP DETECTOR RESPONSIVITY AND TIME CONSTANT

A second way to measure the detector responsivity is by operating the detector closed loop as in its normal operation. During normal operation, the servo loop adjusts the heater power to null out any changes in the input. To measure the responsivity, an offset is added to the error voltage going into the μ processor. The detector is then forced to change the heater power to rebalance the loop. The amount of voltage offset introduced divided by the change in heater power required to rebalance the loop equals the closed loop responsivity.

Figure 8.3 shows a typical closed loop responsivity test for detector no. 1. In this test, the detector is allowed to stabilize at a nominal output level of approximately 20,500 counts. Step offsets of + and - 512 quarter QSEs are then introduced sequentially. The resulting changes in output count levels are then converted to power. The figure shows the output level as a function of sample number or time. The average closed loop responsivity for this test was 1.99 V/W. This compares well with the open loop measurement previously shown of 1.94 V/W.

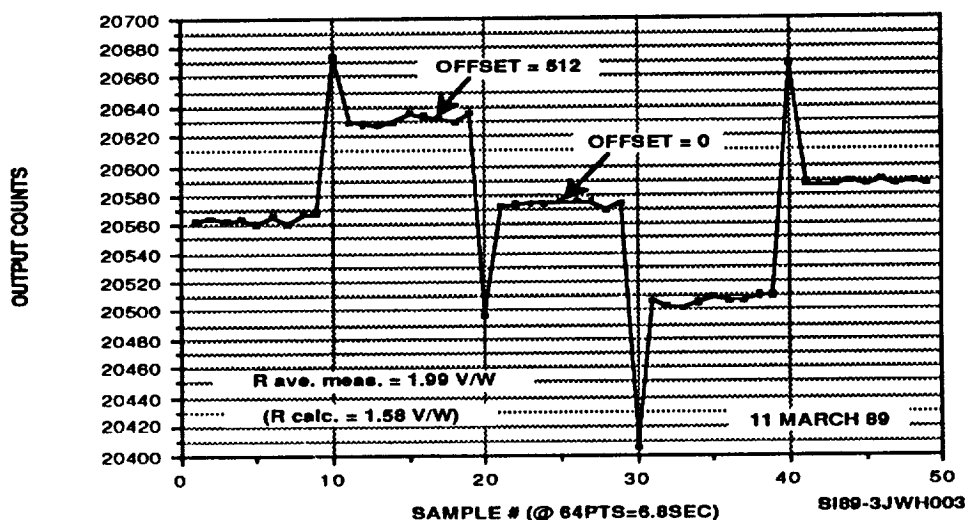


FIGURE 8.3. CLOSED LOOP RESPONSE - DET. 1

8.2.3 DETECTOR CHARACTERIZATION SUMMARY

In order to compare measured values for detector responsivity and time constant with those originally used in the design of the instrument, all of the detector physical parameters must be known. The physical dimensions of each of the cavities and thermal shunts were measured and recorded on data sheets as part of the manufacturing process. Due to the extreme thinness of the electro-formed parts, accurate thicknesses cannot be obtained. A more accurate method using a very accurate mass balance has been postulated for the future.

One of the key parameters in calculating the responsivity is the temperature coefficient, T.C., of the sensor winding. Nickel 272 was selected and used in the

manufacturing of the detectors due to its high T.C.. Published values of T.C. for pure nickel vary from 6,000 to 6,900 PPM. These values are normally obtained by measuring the resistance at 0° C in an ice bath and 100° C in boiling water. As the T.C. is not constant over this large temperature range, these values do not accurately represent the T.C. of the nickel wire at its operating temperature. Figure 8.4 shows the actual measured change in resistance with temperature for the active and reference windings on detector no. 1. A least squares fit to these data points produced a T.C. of 5,450 PPM for the active sensor winding and 5,640 for the reference sensor winding. An average value of 5,600 PPM was thus used for the calculated responsivity of the detectors.

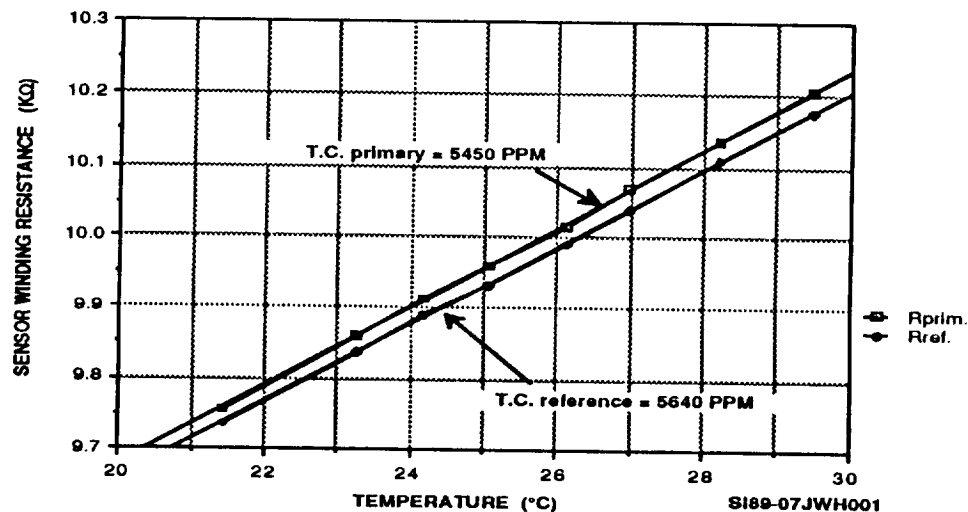


FIGURE 8.4. TEMPERATURE COEFFICIENT MEASUREMENT

A summary of the calculated and measured values of responsivity and time constant is given in Table 8.1. As detector no. 2 underwent rework due to excessive leakage, no open loop measurements were made on this detector.

The average measured responsivity was approximately 35% higher than calculated. This may be due to a higher T.C. than measured and/or inaccuracies in the measurement in the physical measurement of the extremely thin electro-formed parts. The longer time constant agrees with the higher responsivity, but not to the extent measured. The longer time constant is most likely due to the fact that all of the thermal masses such as that of the epoxies, pads, heater wires, etc., have not been included in the thermal mass calculation.

The initial design goal of the detector was to increase the responsivity over prior detectors by an order of magnitude. The responsivity measurements of these detectors show that this goal has been met and exceeded.

TABLE 8.1.

DETECTOR RESPONSIVITY AND TIME CONSTANT

S/N	$R_{CAL.} \left(\frac{V}{W} \right)$	$R_{MEAS.} \left(\frac{V}{W} \right)$		$\Delta\%$	$T_{CAL.} (S)$	$T_{MEAS.} (S)$
		OPEN LOOP	CLOSED LOOP			
1	1.58	1.94	1.99	+25.9	4.7	8.05
2	2.67	--	2.11	--	4.7	--
3	1.85	2.95	2.58	+44.3	4.7	11.3

8.3 CLOSED LOOP DYNAMIC RESPONSE

8.3.1 DETECTOR TRANSFER FUNCTION

A block diagram of the detector control loop was shown previously in Figure 4.4. The output of the detector preamplifier goes through a low pass filter to reduce aliasing caused by sampling. The output signal then goes to a sample/hold and to the A/D converter. The digital error signal is then fed to the μ processor. The μ processor implements the digital control filter which determines the dynamic response of the loop. The output from this digital filter goes to the DAC which holds the voltage for the heater. The power produced in the heater is proportional to the square of this voltage. The detector transfer function thus follows a V^2 form.

The detector transfer function is given Figure 8.5. The dynamic range of the detector was sized based on a maximum radiance of $412 \text{ W/M}^2 \cdot \text{SR}$. This represents an 80% albedo cloud at 245 K temperature. For the largest conceivable field of view this represents a power into the detector of 4.7 mW. The dynamic range of the detector was thus set at 5 mW. When 5 mW is input to the detector no heater power is required. The output of the detector at this point would be minus one-half of the dynamic range of the 16 bit μ processor or minus 32,768 counts. When no power enters the aperture as in space calibration, for example, the detector heater must supply the full 5 mW of power. The detector output level would then be plus 32,768 counts.

A nominal earth scene of 280° K temperature and 10% albedo would produce a radiance of 140 W/M²*SR and a corresponding heater power of 3.4 mW. The output signal at this point would be approximately 22,000 counts. It is thus desired to perform system tests in the general vicinity of this value to represent nominal on orbit conditions.

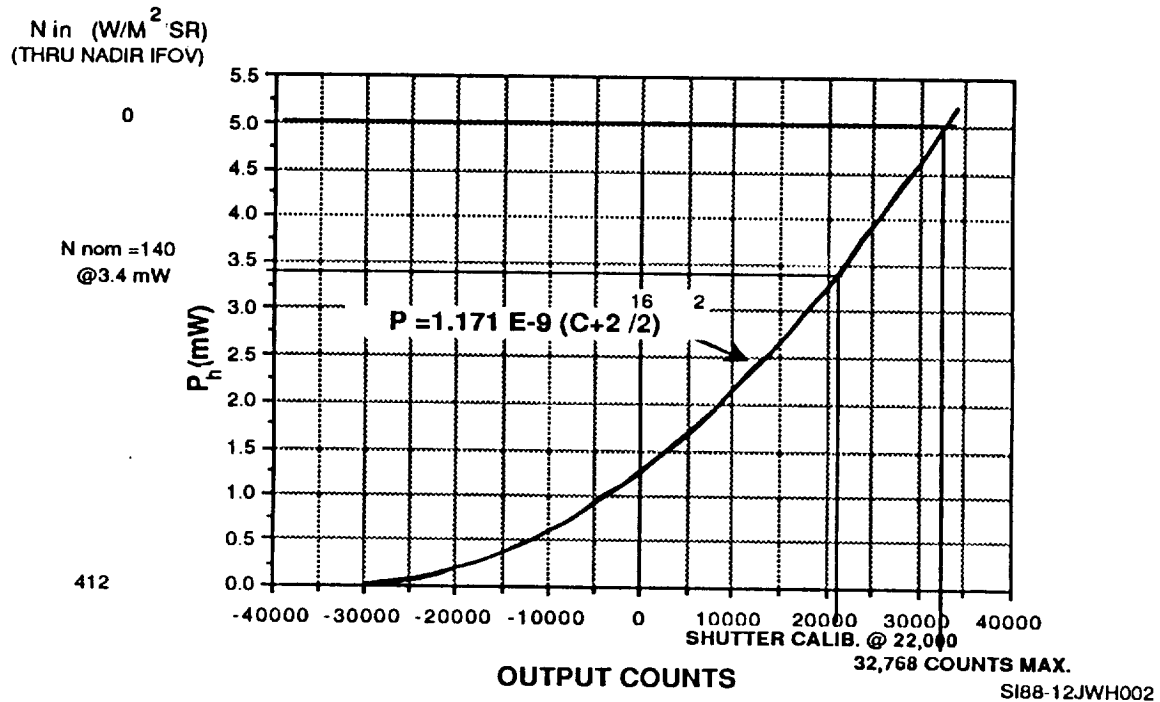


FIGURE 8.5. DETECTOR TRANSFER FUNCTION

The slope of the detector transfer function at any point represents the detector gain. Because of the square law function of the detector heater, the gain is dependent on the operating level. Figure 8.6 shows the detector gain versus the operating point in counts out of the μ processor. At the nominal operating level of 22,000 counts, the gain of the detector is approximately 0.13 μ W/counts. This illustrates the extreme sensitivity of the detector. A variation of 8 counts in the output represents a change in power coming into the detector of only 1 μ W at the nominal operating point. When converted into degrees, one count out of the μ processor represents a temperature change of only 3.1 millionths of a degree Centigrade. This extreme sensitivity of the detector provides a challenge in testing the system in a laboratory and not vacuum environment. Measurement of the long term stability of the detectors is extremely difficult due to the fact that even slight changes in ambient laboratory temperature can produce large changes in output levels.

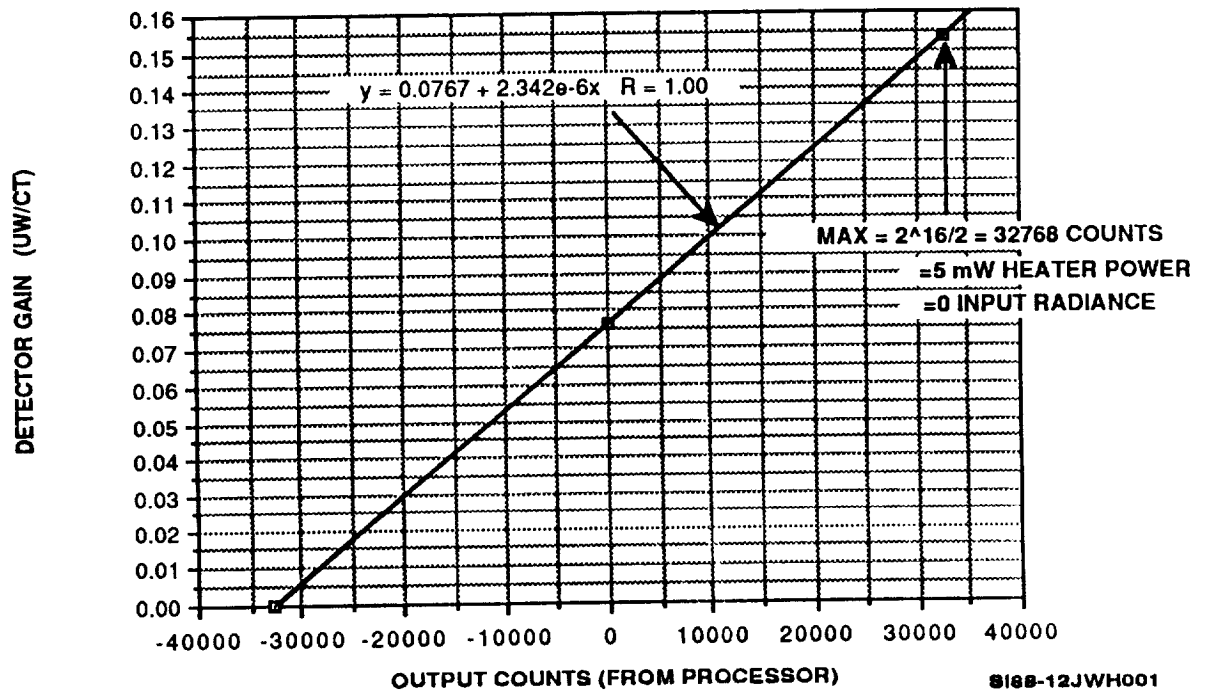


FIGURE 8.6

DETECTOR GAIN VRS. OPERATING POINT

8.3.2 STEP INPUT RESPONSE

With the digit implementation of the control loop, various types of loop compensation filters can be implemented. Figure 8.7 shows a typical response of the detector with the R filter. The parameters for the filter are given at the top of the figure. The graph is a direct screen dump from the Mac II monitor display. It is a real time plot of the detector output voltage (top trace) and the detector error signal (bottom trace) when the shutter is opened to view the blackbody and then closed. When the shutter is opened, the hot blackbody is viewed by the detector. A large negative error signal is produced and the heater voltage is reduced to null out the error signal. As the output level is reduced (top trace) the error signal goes to zero and overshoots slightly before settling. The time scale is 3.36 sec/cm. The settling is approximately 16 seconds for this set of loop parameters.

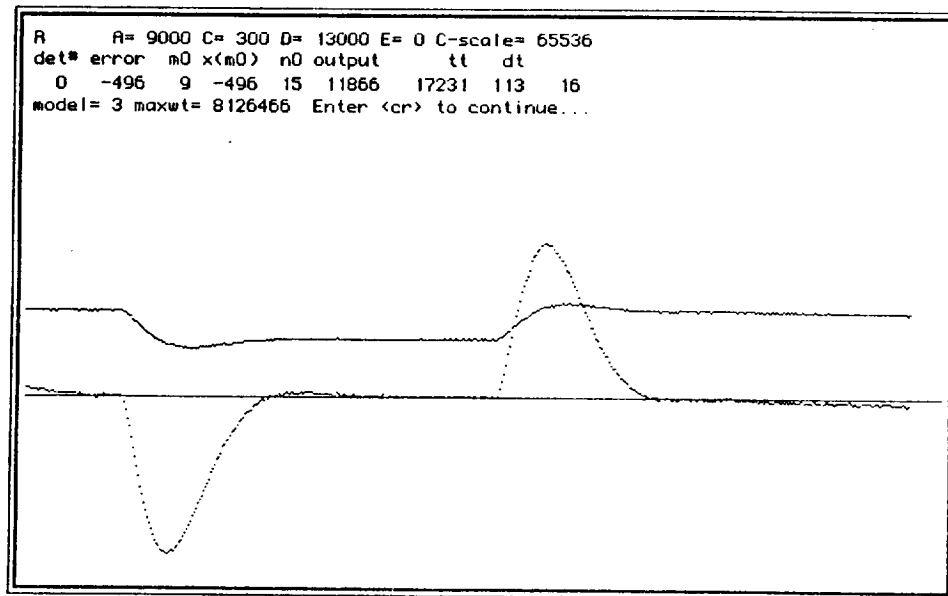


FIGURE 8.7

CLOSED LOOP RESPONSE TO STEP INPUT - DET. 1 REAL TIME MONITOR OUTPUT

As the error signal must always be driven back to zero, it is easier to measure the dynamic response of the loop by monitoring this signal. Figure 8.8 shows an expanded plot of the error signal using the R filter with a nominal set of parameters. These parameters were selected to provide minimal overshoot and good noise performance. The settling time to 1% was 11 seconds which is significantly better than the required time of 28 seconds and only slightly longer than a single detector time constant. A similar response and settling time was obtained with the IIR filter but the parameter adjustments were much more sensitive and difficult to optimize.

The step response represents a step from viewing the calibration shutter at 28° C to the blackbody set at 80° C. This represents a very fast transient which would only be encountered when activating the calibration shutter. During normal on orbit operation, the large field of view of the detector will provide a slow ramp input to the system even when crossing a large radiance change such as a cloud edge or land/water interface. The step response functions thus represent a worst case scenario. The digital loop implementation allows a unique feature to be employed in the flight system. Two sets of control parameters can be utilized. One set for nominal earth viewing and a second set for calibration to respond to the step input provided when the calibration shutter is closed.

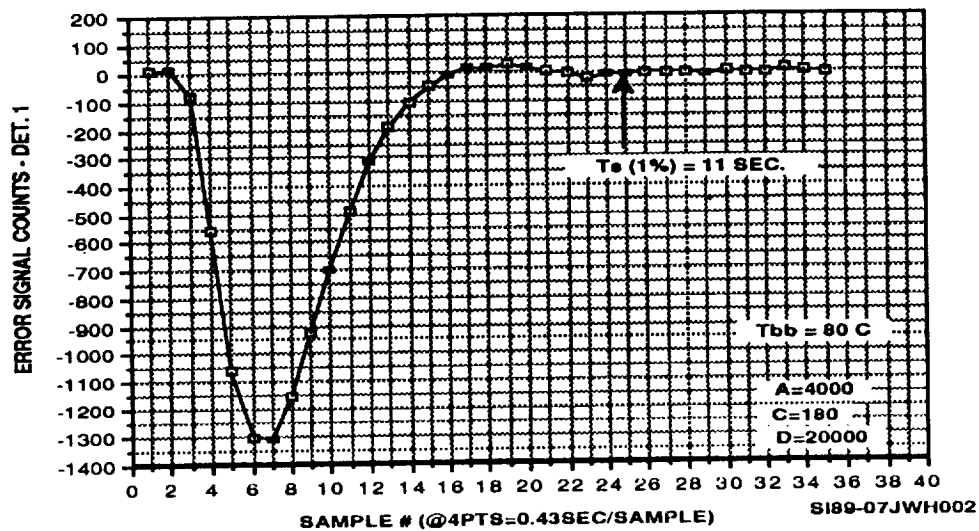


FIGURE 8.8. STEP INPUT RESPONSE - DET. 1

One of the advantages of the digital control loop is that the control parameters can be easily modified. Figure 8.9 shows the effects of changing the overall loop gain on the step response. When the gain is doubled the error signal is limited to less than half its nominal amplitude but the settling time is not improved and the noise level increases. When the loop gain is cut in half, the error signal increases approximately 50% and the settling time increases significantly. Either of these large changes in gain would clearly be unacceptable.

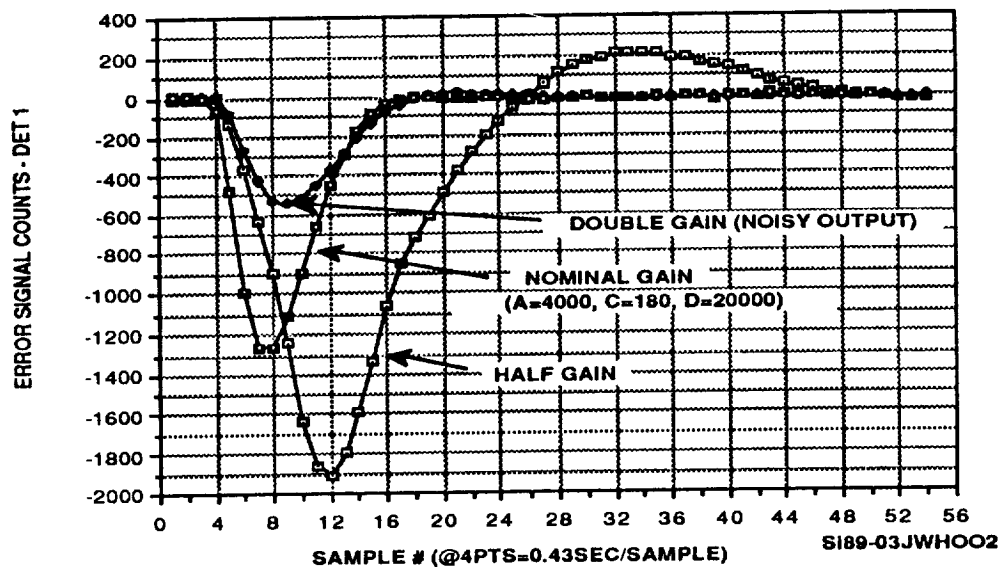


FIGURE 8.9. STEP INPUT RESPONSE VRS. LOOP GAIN

Figure 8.10 shows the effects of adjusting only the integration term of the digital filter. In this particular case, the nominal integration term was set at 180. This provides for a critically damped loop which has the general response desired for this system. Increasing the integration term to 240 decreases the loop damping and allows for two overshoots as shown. Decreasing the integration term to 120 increases the damping such that the loop is overdamped. No overshoot is allowed and the settling time increases significantly. The responses shown represent a step function from the 28° C shutter to the blackbody set at 50° C. In optimizing the control loop response, all constants would be adjusted to provide the optimum transient response.

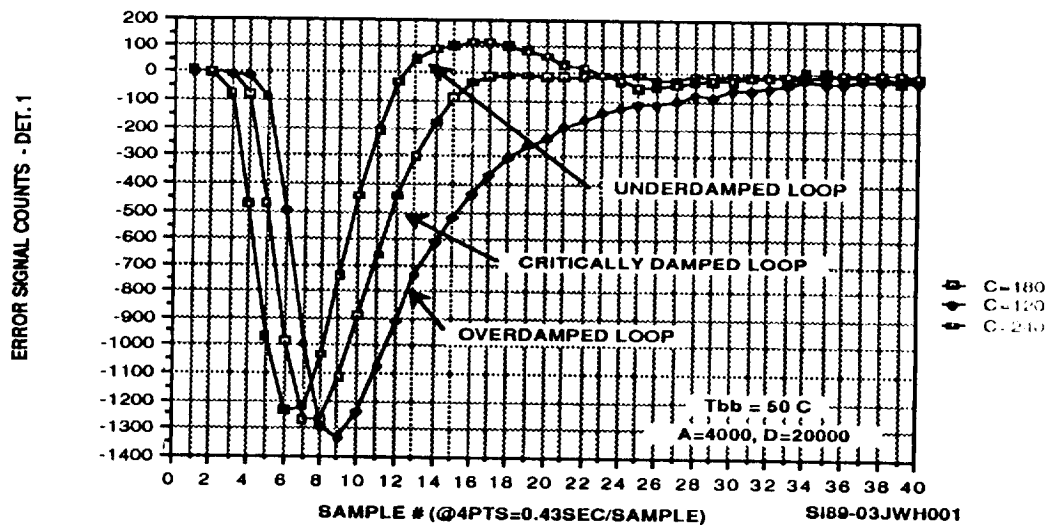


FIGURE 8.10. STEP INPUT RESPONSE VRS. LOOP INTEGRATION

8.4. ELECTRONIC NOISE MEASUREMENTS

8.4.1 NOISE MEASUREMENTS

The primary noise sources are the Johnson noise in the four bridge resistors, the preamplifier input noise, the quantization noise and the DAC linearity. Less important noise sources include the shot noise on the preamplifier bias current and the Johnson noise on the heater wire current. Typical time outputs of two of the detectors are shown in Figure 8.11. For these noise tests, the detectors were capped and allowed to stabilize at a constant output level. Detector 2 had a 1 sigma noise of 74 counts and detector 3 of 68 counts. Without smoothing of samples, the average noise was 71 counts or approximately 9 μ W at the nominal operating level of 22,000 counts. As the initial error budget allocation for the one sigma noise was 220 counts, the performance far exceeds the design requirements.

The development software contains the ability to average any number of samples and also determine the statistics on the averaged value. As the control loop operates at a

high sample rate and it is envisioned to average many samples to reduce the noise, it is of interest to determine if the noise is reduced by the theoretical square root of the number of samples. The middle part of the chart shows the resultant outputs when 16 samples are averaged and the right part of the curve shows the resultant outputs after averaging 100 samples. Figure 8.12 plots the noise reduction factor actually measured versus the theoretical value. It can be seen that the reduction is in general agreement with the theoretical values.

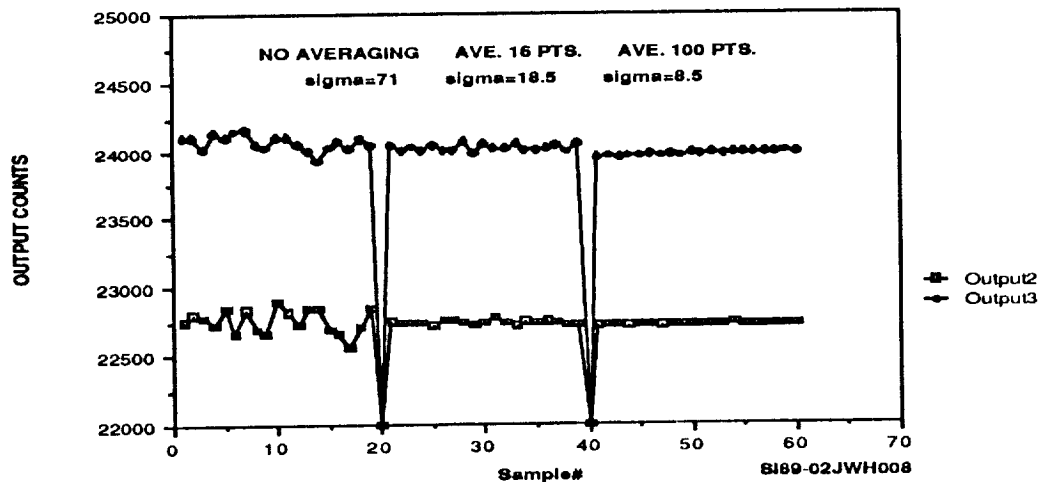


FIGURE 8.11

TIME OUTPUTS AFTER AVERAGING

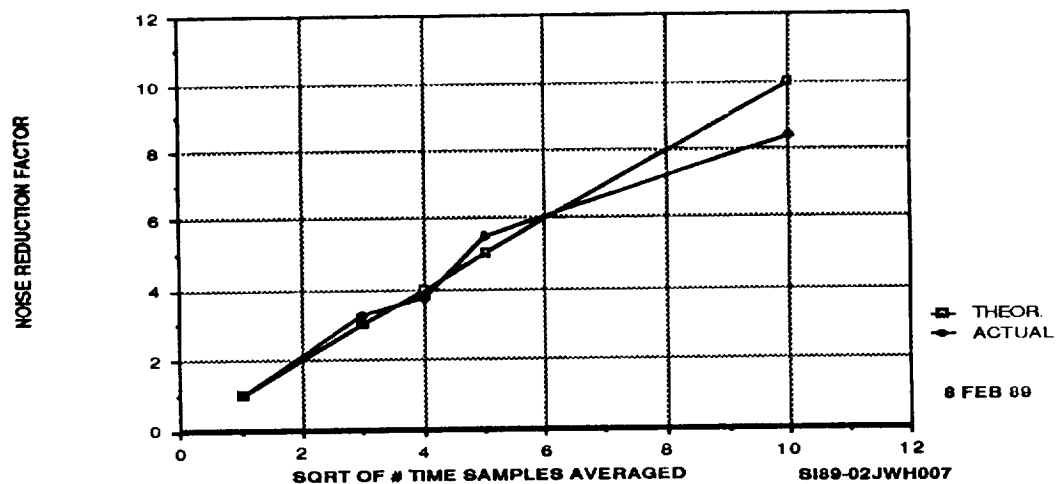


FIGURE 8.12

NOISE REDUCTION BY SAMPLE AVERAGING

8.4.2 NOISE PSD

An FFT program was incorporated in the development software to obtain PSDs of the detector outputs and insure that no unique noise frequency components are present. Figure 8.13 shows a sample PSD for detector 1. As the number of samples used is relatively small, the spectrum is not perfectly flat but does not contain any large frequency components at isolated frequencies. PSDs taken on the other detectors gave similar results. The noise can therefore be assumed to be approximately Gaussian. The results of both of these tests indicate that smoothing output data samples will have the desired effect of reducing the noise level by approximately the square root of the number of samples.

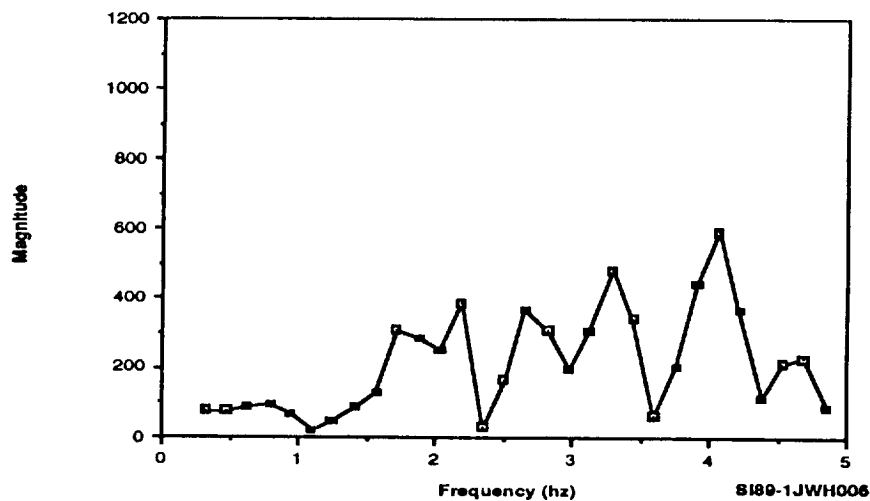


FIGURE 8.13

NOISE PSD - DET. 1 CAPPED

8.4.3 NOISE VERSUS TEMPERATURE

A test was performed to determine if the noise level in the detectors would increase as the detector temperature increased. The servo control loop for the test fixture heatsink was increased from 26 to 34° and noise measurements were made at each temperature level for all three detectors. The results are shown in Figure 8.14. Although a very slight increase in noise level was measured, the increase represents an insignificant change as the heatsink block will be controlled to approximately 0.02° C during on orbit operation.

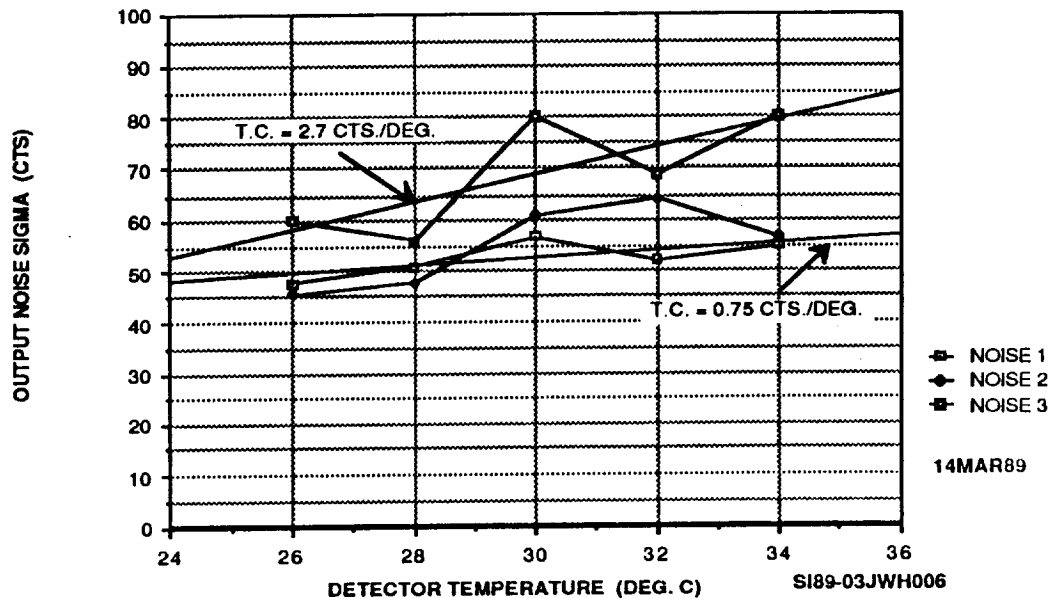


FIGURE 8.14

NOISE VRS. TEMPERATURE

8.4.4 NOISE SUMMARY

Although the measured noise value of approximately 70 counts is far better than the allocated value of 220 counts, it was still of interest to try and determine which were the primary noise components and whether these agreed with the original noise model. Two tests were performed to differentiate between detector/preamplifier noise sources and digital electronics noise sources. In the first test, the noise was measured on all three detectors and then cables 1 and 3 were interchanged going to the electronics box. In both sets of measurements, the noise in channel 3 was approximately three times the noise in channel 1 thus indicating that the primary noise sources were in the electronics box (and most likely due to the grounding scheme used in the electronics box). Following this test, another test was run in which a detector module with a preamplifier but no detector was inserted into channel 3. Once again, there was no significant difference in the noise measured in channel 3. The predominant noise sources are, therefore, in the digital electronics unit as shown in the original precision analysis. Because the quantization noise is small with the 16 bit processor, the largest noise source appears to be the DAC.

8.5 DETECTOR TO DETECTOR PATTERN NOISE

In a mosaic instrument containing a large number of detectors, another noise source is detector to detector pattern noise. Even with the tightest manufacturing controls no two detectors can be manufactured with the identical dimensions. Thus, each detector will read slightly differently when viewing the same scene. These differences can be adjusted by calibration, if need be. If they are, however, of the same approximate level as the electronics noise, they need not be corrected for and will average out after summing the outputs from all of the detectors in the array. This summing or integration of all the angular measurements will be done on the ground over a period of time in order to determine the total flux coming off each ground target area.

In order to measure the pattern noise of the three detectors in the test set up, two methods were used. In the first method a step input was put into each detector sequentially by means of the blackbody and the shutter. This method allows a large step change in temperature but does not produce accurate results because of the elapsed time between moving the blackbody to each detector and allowing the detector and test fixture temperature to stabilize.

In the second method, step inputs were put into all three detectors simultaneously by opening the shutter and allowing all three detectors to simultaneously view a large cold plate. Although the cold plate did not provide a very large change in temperature, it did allow simultaneous measurement of the three detectors. The outputs of the three detectors as a function of time (or sample number) are shown in Figure 8.15. The one sigma difference in the three readings is on the order 8.8 counts or $1.1 \mu\text{W}$. The original error budget allowed for 200 counts of pattern noise. These excellent results indicate that pattern noise will be an insignificant noise factor in the final instrument.

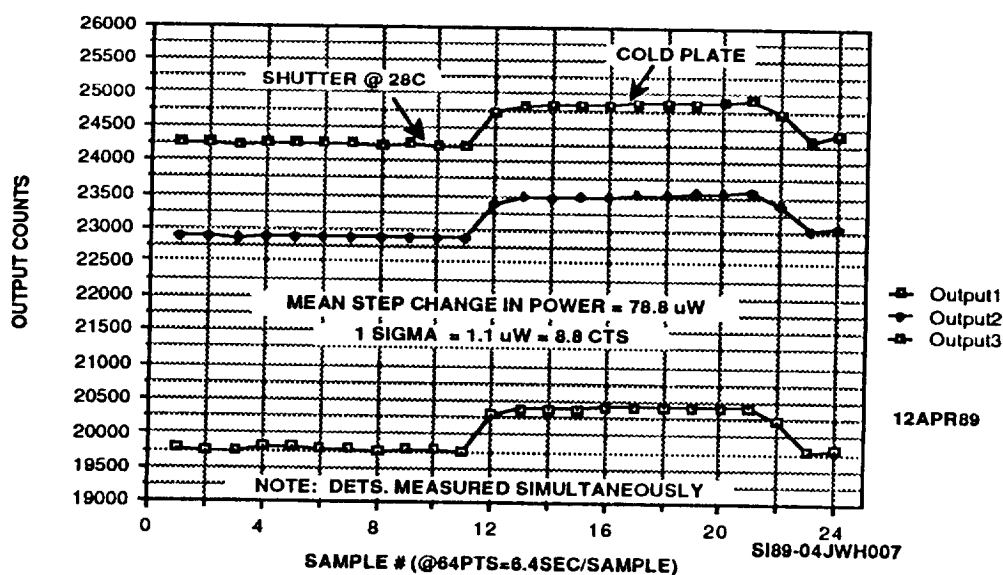


FIGURE 8.15. DET. TO DET. PATTERN NOISE WITH COLD PLATE

8.6 LONG TERM STABILITY

One of the most critical parameters for the final performance of the instrument is the long term stability. This determines how often shutter calibrations must be performed. The primary sources of drift are the bridge resistors, the preamplifier output and offset drifts, the heater resistor drift and the DAC drifts. The largest source of drift is the bridge resistors with a value of $0.1 \text{ PPM}/^{\circ} \text{C}$. This is the specified value for the Vishay VHD 200 matched resistors, which were used because they were the most stable resistors available.

Because of the extreme sensitivity of the detectors drift measurements were made at night when the lab was unoccupied and temperature fluctuations were minimized. In spite of this, the cooling of the laboratory was sensed by the detectors. The front of each detector was capped for the stability tests and was located inside the heatsink which was actively controlled to 28°C . The primary cavity, therefore, saw a cap temperature that was held close to 28°C . The rear of the module was exposed to ambient air in the laboratory even though enclosed with insulation material. As the laboratory cooled down at night the rear cover of the detector modules cooled slightly with it. The detector control loop sensed the imbalance and decreased the output voltage to the heater accordingly. The drift rate during this period was on the order of 1 to 3 counts/minute. In the morning when the laboratory was again occupied and warmed up, the output signal increased accordingly.

The most meaningful method for obtaining long term stability measurements was to run the test over a period of days while the laboratory was unoccupied. Figure 8.16a shows the results of such a long term test. The output level from detectors 1 and 3 is plotted in counts as a function of sample number over a period of 10 days. Each sample represents the average of 33,804 samples which equals exactly one hour in time. For this test, two modifications were made to the detectors. A new rear thermal cap was manufactured out of pure copper and installed in detector 1 to provide better thermal conductivity to the heatsink. The use of copper instead of aluminum for the inner parts that connect to the heatsink is a design improvement that will be considered on future detectors. On detector no. 3 a heater element was installed on the thermal reference cap and actively controlled to 0.005°C to try and reduce temperature fluctuations. Due to the extreme sensitivity of the detector this level of temperature control was found to be not accurate enough to improve the stability of the detectors.

The daily fluctuations due to the heating and cooling of the laboratory result in minimums at approximately 8 am and maximums at approximately 6 pm each evening. To explain the varying amplitude in the daily cycles minimum and maximum daily air temperatures in the San Diego area were obtained from the National Weather Service for this ten day period. These values are plotted in Figure 8.16b and demonstrate the same general trend as the fluctuations observed in the lab by the detectors.

A straight line regression to the data points gives an estimate of the long term stability that could be expected in a space environment with no ambient temperature

fluctuations. For detector no. 1 the straight line interpolation gives a drift rate of approximately +0.013 counts per minute. For detector no. 3 the rate is approximately -0.017 counts per minute. The average drift rate is thus 0.015 counts or 0.002 μW per minute or 0.12 μW per hour. These rates show excellent stability which exceed by 2 orders of magnitude the original design goal of 5.3 counts per minute allocated in the original error budget. Vacuum testing will be required to produce more accurate long term stability measurements.

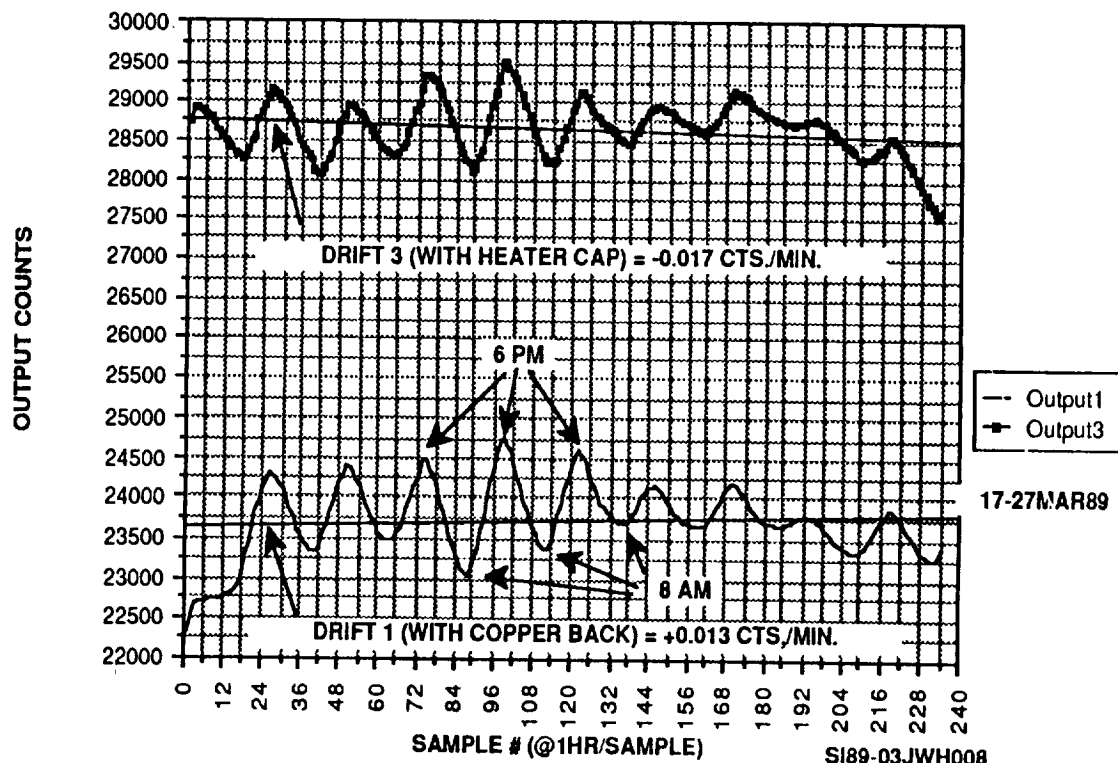


FIGURE 8.16a. 10 DAY DRIFT TEST

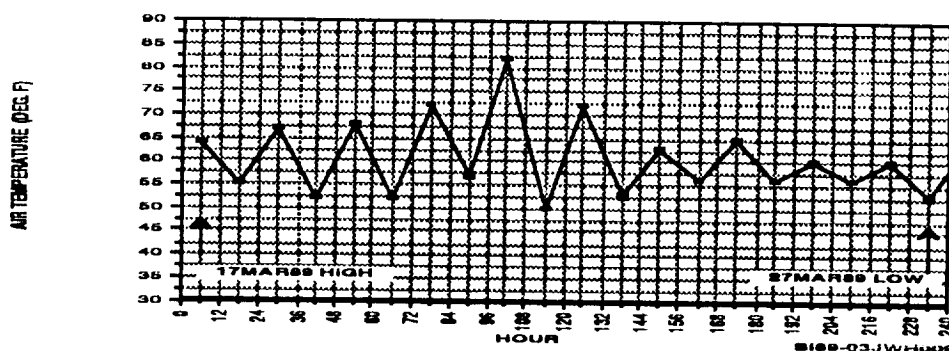


FIGURE 8.16b. MINIMUM/MAXIMUM TEMPERATURES AT SAN DIEGO A.P.

8.7 CROSSTALK

In a mosaic array sensor a large signal put into one detector can cause a spurious signal in an adjacent or nearby detector. This can be caused by electrical, optical, or thermal crosstalk and generally is a combination of the three. Two tests were performed to determine the approximate magnitude of this crosstalk. In the first test, a light source was used to measure only the electrical crosstalk. As the detectors are not located in close proximity as they would be in a flight instrument, the optical crosstalk cannot be measured. The light source was set to provide a step input of approximately 3,500 counts. Figure 8.17a shows the step input of light to detector no. 1 and the simultaneous time profiles from detectors 2 and 3. An expanded scale plot of the outputs from detectors 2 and 3 is shown in Figure 8.17b. No measureable crosstalk can be seen in the results. The crosstalk is thus significantly lower than the inherent electronic noise. If it is assumed that a change in output of approximately one third of a division or three counts could be detected, then the electrical crosstalk is less than approximately 0.1%.

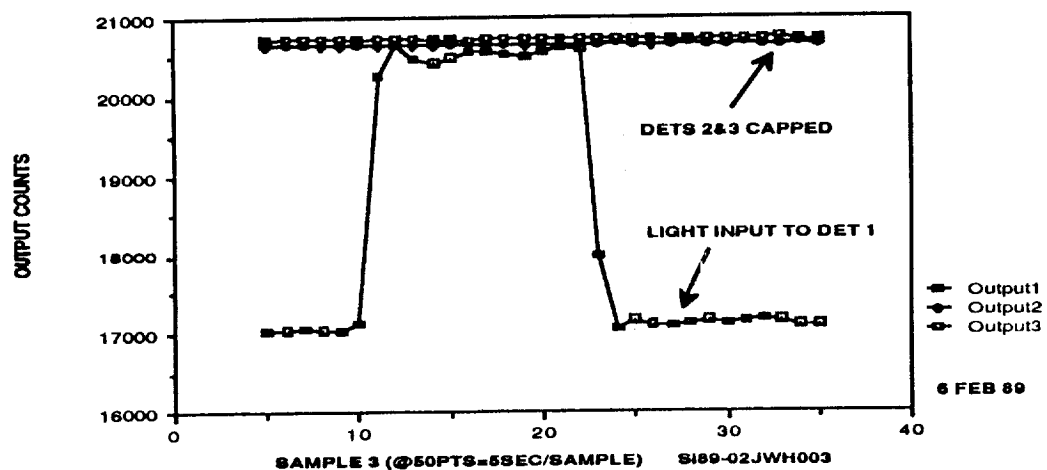


FIGURE 8.17a. ELECTRICAL CROSSTALK TEST

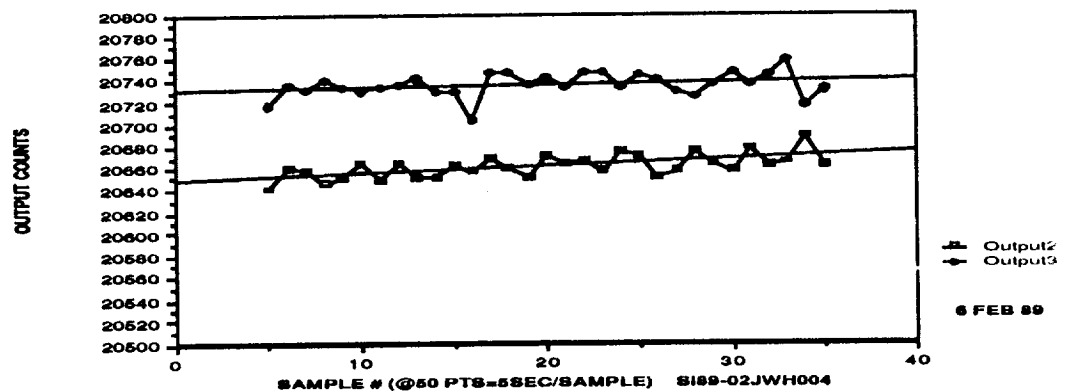


FIGURE 8.17b. DET. 2 & 3 OUTPUTS DURING CROSSTALK TEST

In an earth radiation instrument the primary mechanism for crosstalk between detectors would most likely be thermal crosstalk due to the extreme thermal sensitivity of the detectors. The flight instrument will be designed with a massive heatsink to minimize such crosstalk between the detectors. The test fixture was not designed to have this capability. In spite of this, it was of interest to make a total crosstalk measurement using the three detectors in the existing test fixture.

For this total crosstalk test the blackbody was used and set at close to its maximum temperature to provide the largest possible step input of temperature to detector no. 1 and see if any changes in detectors 2 and 3 could be found. The blackbody was set at 220° C and input to detector no. 1. After the reading stabilized at approximately -11,000 counts, the shutter at 28° C was closed. The resulting output signals from all 3 detectors is shown in Figure 8.18a. The expanded output signals from detectors 2 and 3 are plotted in Figure 8.18b. A very small change in output level can be detected in detectors 2 and 3 on the order of 0.22%. This value was calculated by using the actual numerical data points stored in the computer. It is expected that with the final instrument configuration, this low value of total crosstalk will be reduced even further.

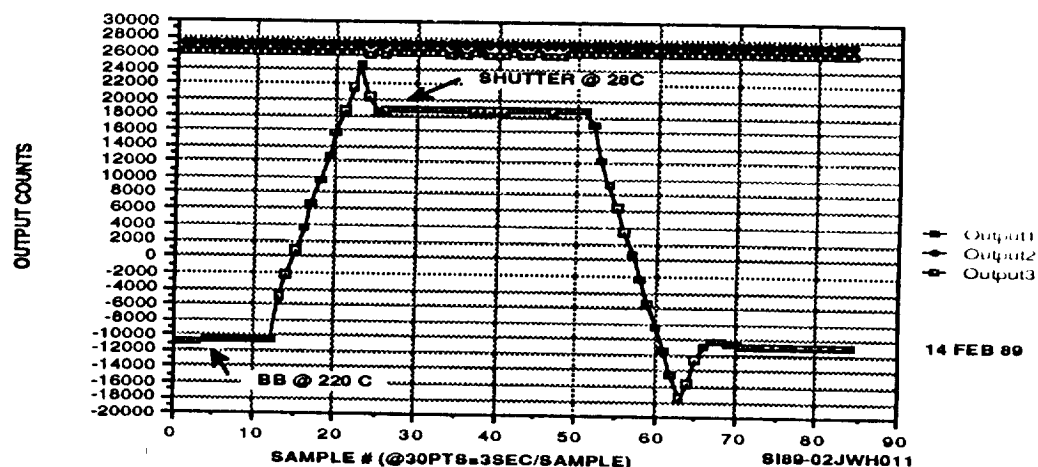


FIGURE 8.18a. CROSSTALK TEST

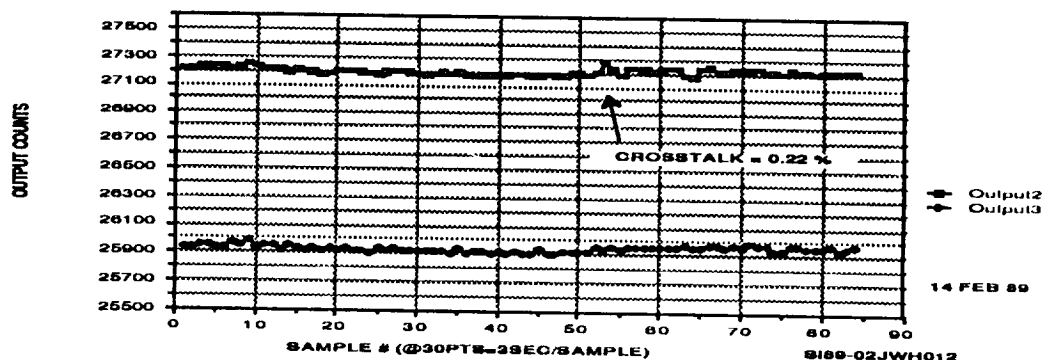


FIGURE 8.18b. CROSSTALK DETECTOR OUTPUTS

8.8 ROM ABSOLUTE CALIBRATION

As the dual cavity detectors are actually measuring differences in power it is desirable at some point to perform an absolute calibration. This will eventually be done in a vacuum by comparing the output of the detectors with a standard such as a WRR (World Radiometric Reference) detector viewing a known source such as the sun. It was, however, desired to obtain an ROM (Rough Order of Magnitude) check on this absolute calibration in the laboratory. The goal was to use the blackbody and determine if the calculated step change from the blackbody to the shutter temperature would be within 20-30% of the absolute step change measured by the detector. With this test, the blackbody was once again set at 220° C. A one centimeter field aperture was used in the test fixture. The measured change in received power from the shutter at 28° C at the blackbody at 220° C was 2.536 mW. The theoretical change in power calculated from the field of view, collecting area, and blackbody temperature was 2.223 mW. The measured value was within 12.5% of the theoretical value and was thus in good agreement for an ambient air test.

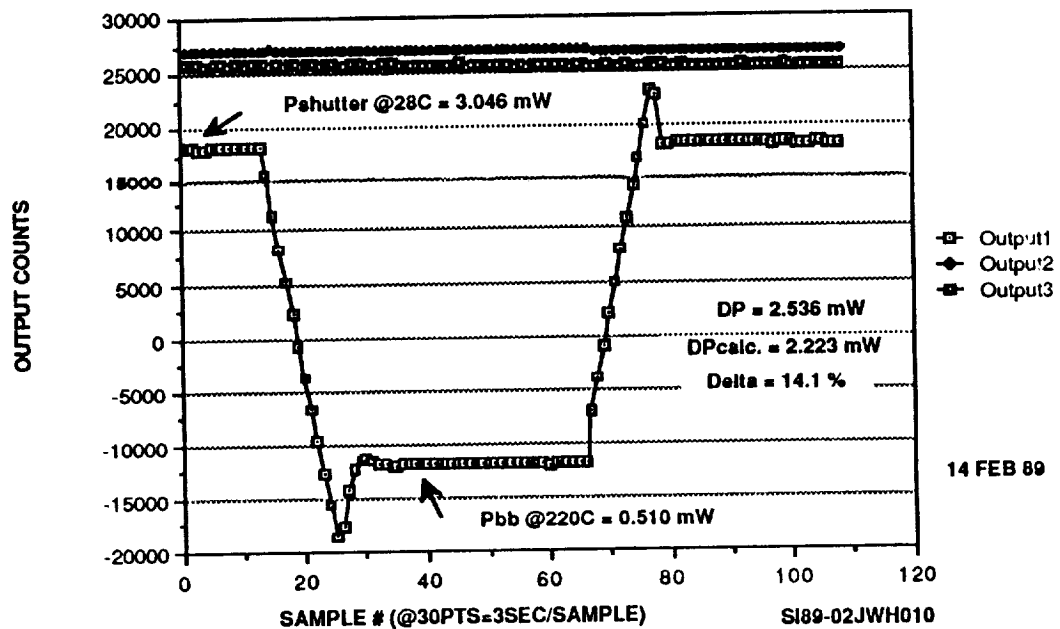


FIGURE 8.19

ROM ABSOLUTE CALIBRATION

8.9 PERFORMANCE SUMMARY

A summary of the test results and the original design requirements as derived in the original error budgets is shown in Table 2. It can be seen that all of the test results meet or better the required values. It is significant to note that the long term drift which is the most important system parameter significantly exceeds the original design requirements.

TABLE 8.2
INSTRUMENT PERFORMANCE SUMMARY

NO.	PERFORMANCE PARAMETERS	REQUIREMENT	AVE. MEASURED VALUE
1	RESPONSIVITY	1.5 V/W	2.3 V/W
2	NOISE -1 SIG.	220 CTS	71 CTS
3	DET. TO DET. VAR. -1 SIG.	200 CTS	8.8 CTS
4	DRIFT	5.3 CTS/MIN.	0.015 CTS/MIN.
5	CROSSTALK	TBD	0.2%
6	SETTLING TIME	28 SEC.	11
7	DATA DUTY CYCLE	95%	98%

NOTES: NOISE AT INPUT TO μ P IS ONLY = $\pm 1-3$ COUNTS

SI89-01JWH017

9.0 CONCLUSIONS

All of the original objectives of the SBIR Phase I and Phase II projects have been successfully fulfilled. The ERA breadboard hardware was designed, manufactured, and tested. The digital control loop worked perfectly and demonstrated the design flexibility expected. The detectors achieved even greater responsivity than the theoretical design value. Very encouraging was the fact that the long term stability appears to be over 2 orders of magnitude better than that budgeted for. Detector stability is one of the most important performance parameters. The test results indicate that the detectors may have commercial use as absolute references for laboratory and inflight calibration of other instruments. The overall instrument concept for the ERA has thus been demonstrated to be feasible and ready for development and a precision on the order of 0.5% appears possible.

10.0 RECOMMENDATIONS

The fabrication and testing of the breadboard detectors and electronics leads to the following recommendations:

1. The use of copper parts for the front baffle assembly and rear thermal cap should be investigated to provide better thermal conductivity to the main instrument heatsink.
2. Extra layers of epoxy should be placed beneath the sensor windings to reduce leakage.
3. An improved detector lead feedthrough should be designed.
4. The long term stability of the detector should be accurately measured in a vacuum environment.
5. The detector should undergo absolute calibration against a WRR detector.
6. A commercial version of the detector should be developed as an absolute radiometry standard for laboratories and space chambers.
7. Work should proceed on the thermal analysis and modelling of the instrument and the mechanical design of the integral heatsink.
8. A detailed design of the calibration shutter and its drive mechanism should begin.
9. The development of the flight model should be initiated.